Draft version October 1, 2021
Typeset using LaTeX twocolumn style in AASTeX63

A Tale of Two Type Ia Supernovae: The fast-declining siblings SNe 2015bo and 1997cn

W. B. Hoogendam[1,2] C. Ashall[1] L. Galbany[3] B. J. Shappee[1] C. R. Burns[4] J. Lu[5] M. M. Phillips[6] E. Baron[7,8] E. Y. Hsiao[5] N. Morrell[6] M. D. Stritzinger[9] N. B. Suntzeff[10] F. Taddia[9] D. R. Young[11] J. D. Lyman[12] S. Benetti[13] P. A. Mazzali[14,15] M. Delgado Mancheño,[16] R. González Díaz,[17,3] and S. Muñoz Torres[16]

[1] Institute for Astronomy, University of Hawaii, 2680 Woodlawn Drive, Honolulu, HI 96822, USA
[2] Department of Physics and Astronomy, Calvin University, Grand Rapids, MI 49546, USA
[3] Institute of Space Sciences (ICE, CSIC), Campus UAB, Carrer de Can Magrans, s/n, E-08193 Barcelona, Spain.
[4] Observatories of the Carnegie Institution for Science, 813 Santa Barbara St., Pasadena, CA 91101, USA
[5] Department of Physics, Florida State University, 77 Chieftan Way, Tallahassee, FL 32306, USA
[6] Carnegie Observatories, Las Campanas Observatory, Casilla 601, La Serena, Chile
[7] 8Homer L. Dodge Department of Physics and Astronomy, University of Oklahoma, 440 W. Brooks, Rm 100, Norman, OK 73019-2061,USA
[8] Hamburger Sternwarte, Gojenbergsweg 112, D-21029 Hamburg, Germany
[9] Department of Physics and Astronomy, Aarhus University, Ny Munkegade 120, DK-8000 Aarhus C, Denmark
[10] George P. and Cynthia Woods Mitchell Institute for Fundamental Physics & Astronomy, Texas A&M University, Department of Physics and Astronomy, 4242 TAMU, College Station, TX 77843, USA
[11] Astrophysics Research Centre, School of Mathematics and Physics, Queen's University Belfast, Belfast BT7 1NN, UK
[12] Department of Physics, University of Warwick, Gibbet Hill Road, Coventry CV4 7AL, UK
[13] INAF - Osservatorio Astronomico di Padova, Vicolo dell'Osservatorio 5, I-35122 Padova, Italy
[14] Astrophysics Research Institute, Liverpool John Moores University, IC2, Liverpool Science Park, 146 Brownlow Hill, Liverpool L3 5RF, UK
[15] Max-Planck-Institut für Astrophysik, Karl-Schwarzschild Str 1, D-85748 Garching, Germany
[16] Departamento de Física Teórica y del Cosmos, Universidad de Granada, E-18071 Granada, Spain
[17] Instituto Nacional de Astroísica, Óptica y Electrónica (INAOE), 72840 Tonantzintla, Puebla, Mexico.

ABSTRACT

We present optical and near-infrared photometric and spectroscopic observations of the fast-declining Type Ia Supernova (SN) 2015bo. SN 2015bo is under-luminous ($M_B = -17.50 \pm 0.13$ mag) and has a fast-evolving light curve ($\Delta m_{15}(B) = 1.91 \pm 0.01$ mag and $s_{BV} = 0.48 \pm 0.01$). It has a unique morphology in the $V-r$ color curve, where it is bluer than all other SNe in the comparison sample. A ^{56}Ni mass of $0.17 \pm 0.03\ M_\odot$ was derived from the peak bolometric luminosity, which is consistent with its location on the luminosity-width relation. Spectroscopically, SN 2015bo is a Cool SN in the Branch classification scheme. The velocity evolution measured from spectral features is consistent with 1991bg-like SNe. SN 2015bo has a SN twin (similar spectra) *and* sibling (same host galaxy), SN 1997cn. Distance moduli of $\mu = 34.36 \pm 0.01$ (stat) $\pm$ 0.13 (sys) mag and $\mu = 34.37 \pm 0.04$ (stat) $\pm$ 0.12 (sys) mag were derived for SN 2015bo and SN 1997cn, respectively. These distances are consistent at the $0.06-\sigma$ level with each other, and are also consistent with distances derived using surface-brightness fluctuations and redshift-corrected cosmology. This suggests that fast-declining SNe could be accurate distance indicators which should not be excluded from future cosmological analyses.

Keywords: Supernovae

1. INTRODUCTION

Type Ia supernovae (hereafter SNe Ia) have many astrophysical and cosmological applications. They are one of the major sources of metal enrichment (Raiteri et al. 1996), used as standard candles (e.g. Phillips 1993; Phillips et al. 1999; Burns et al. 2018), and help to determine the acceleration rate of the universe (e.g. Riess et al. 1998; Perlmutter et al. 1999). SNe Ia have additional applications: they continue to be used to calculate the Hubble constant (e.g. Riess et al. 2016; Burns et al. 2018; Khetan et al. 2021), improve constraints on the equation-of-state for dark energy w parameter (e.g. Betoule et al. 2014; Scolnic et al. 2018), and investigate the distribution of dark matter in galaxies (e.g. Feindt et al. 2013).

It is now apparent that SNe Ia are not an entirely uniform class of objects; rather, there are a growing number of sub-types. These include: the over-luminous 1991T-like SNe Ia (e.g., Filippenko et al. 1992a; Phillips et al. 1992); 2003fg-like SNe Ia which are brighter in the NIR and have long rise times (e.g., Howell et al. 2006; Hicken et al. 2007; Hsiao et al. 2020; Ashall et al. 2021; Lu et al. 2021); 2002cx-like SNe Ia show light curves that are both broad and faint (e.g., Li et al. 2003; Foley et al. 2013); 2006bt-like SNe Ia are with broad, slowly declining light curves seen in high luminosity SNe Ia, yet they lack a prominent secondary maximum in the i-band as seen in low luminosity SNe Ia (e.g., Foley et al. 2010a); 2002ic-like SNe Ia that exhibit Balmer emission lines found in Type IIn core-collapse SNe (Hamuy et al. 2003); and lastly, 1991bg-like SNe Ia are sub-luminous (e.g., Filippenko et al. 1992b; Leibundgut et al. 1993; Turatto et al. 1996). In addition to these broad categories, there are also several types of SNe Ia that straddle the boundaries between these sub-types. One of these is the so-called transitional SNe Ia. Transitional SNe bridge the gap between normal and 1991bg-like SNe. They tend to be fast-declining and exhibit other features of 1991bg-like SNe, but are not entirely consistent with the 1991bg-like SNe classification. Examples of transitional objects include SN 1986G, SN 2003hv, SN 2004eo, SN 2007on, SN 2011iv, and iPTF13ebh (e.g., Phillips et al. 1987; Leloudas et al. 2009; Pastorello et al. 2007; Gall et al. 2018; Ashall et al. 2018; Hsiao et al. 2015). For a full review of all sub-types, see Taubenberger (2017).

Roughly 18% of all SNe Ia are considered 1991bg-like SNe (Li et al. 2011). It is hotly debated if they are produced by Chandrasekhar (Ch) mass or sub-Ch mass explosions (e.g., Höflich et al. 2002; Stritzinger et al. 2006; Blondin et al. 2018). In addition to being sub-luminous ($M_B > -18$ mag; Taubenberger 2017), 1991bg-like SNe differ in many ways compared to normal SNe Ia. For example, 1991bg-like SNe light curves differ photometrically with their faster rise and decline and less luminous peak (hence the classification as sub-luminous). Whereas other supernovae have either a shoulder or a second maximum in the i-band, 1991bg-like SNe have neither (Ashall et al. 2020). However, it is in their spectroscopic properties where 1991bg-like SNe differ the most: they have noticeably stronger Ti II and O I features than other types, and also have a strong Si II feature at 5972 Å (Nugent et al. 1995; Benetti et al. 2005).

One might suspect that, due to their astronomical importance, SNe Ia would be well understood; yet the progenitor systems of SNe Ia, their explosion details, and the underlying physical interpretation of the empirical relationships are not fully known despite decades of research. SNe Ia are agreed to come from the explosion of at least one carbon-oxygen (C-O) white dwarf (WD) (Hoyle & Fowler 1960). However, there are several potential progenitor scenarios that could produce a SN Ia. These are: the single degenerate (SD) scenario which consists of a single C-O WD and a non-degenerate companion star (Whelan & Iben 1973; Livne 1990; Nomoto et al. 1997), the double degenerate (DD) scenario which consists of two C-O WDs (Iben & Tutukov 1984; Webbink 1984), and the triple/quaternary scenario which consists of two C-O WDs in a system with at least one other companion star (Thompson 2011; Pejcha et al. 2013; Shappee & Thompson 2013).

For each of these scenarios, there are a variety of viable explosion mechanisms and ejecta masses. A C-O WD may accrete mass from a companion star until it approaches the Chandrasekhar limit, where compressional heating in the center of the explosion can start a thermonuclear disruption (e.g., Diamond et al. 2018). This can occur in the SD (Whelan & Iben 1973) or DD scenarios (Piersanti et al. 2003). Alternatively, a sub-Chandrasekhar mass C-O WD may accrete a surface helium layer which can detonate and produce an inward-moving shock wave and total disruption of the WD (Nomoto 1980; Woosley & Weaver 1994; Hoeflich & Khokhlov 1996). This is possible in both the SD or DD scenarios. A sub-Chandrasekhar mass explosion may also result from a merger between two C-O WDs (whose combined mass does not exceed the Chandrasekhar limit; van Kerkwijk et al. 2010). Another explosion mechanism in the DD progenitor scenario is where two white dwarfs violently merge as a result of angular momentum loss from gravitational radiation. The heat generated from merging provides the necessary spark for the powder keg (Iben & Tutukov 1984). Finally, the head on collision of two WDs, which may be in a multiple system, can produce a SNe Ia where the explosion is triggered by a detonation wave (Rosswog et al. 2009; Raskin et al. 2009; Thompson 2011; Katz & Dong 2012; Kushnir et al. 2013; Pejcha et al. 2013; Dong et al. 2015; Mazzali et al. 2018).

One of the most important empirical relationships that SNe Ia follow is the luminosity-width relationship. This study utilizes the luminosity-width relation in two representations. First, by examining the difference in magnitude in B-band from maximum light ($t(B)_{\max}$) to fifteen days past maximum (the $\Delta m_{15}(B)$ quantity) against the absolute B-band magnitude (M_B) (Phillips 1993; Phillips et al. 1999). Second, by examining the time difference between the time of B-band and

$B-V$ maximum normalized by 30 days (s_{BV}) versus M_B (Burns et al. 2014). For both of these relationships, more luminous objects have broader light curves, however, s_{BV} is a better indicator for fast-declining objects such as 1991bg-like SNe because Δm_{15}(B) is not a reliable measure of the decline rate for values greater than 1.7 mag (Phillips 2012; Burns et al. 2014; Gall et al. 2018). The physical understanding of the luminosity-width relation lies in the amount of ^{56}Ni synthesized in the explosion (Nugent et al. 1995). More luminous objects have more ^{56}Ni (Stritzinger et al. 2006), which provides more line opacity and increases the diffusion time scales in the ejecta. This causes broader light curves (e.g., Mazzali et al. 2007). For the least luminous objects, the ^{56}Ni mass will be lower and line opacity small which causes quickly evolving light curves.

SNe Ia serve as excellent tools to calculate extra-galactic distances (Phillips 1993; Hamuy et al. 1996; Phillips et al. 1999) after correcting for the luminosity-width relationship (c.f. Hamuy et al. 1996). However, analyses of distances for SNe Ia in galaxies with low redshifts ($z \leq 0.1$) have additional variance due to peculiar velocities and host galaxy bulk flows relative to cosmological expansion. This can be avoided by comparing SNe Ia that explode in the same galaxy (and thus have the same bulk flow and peculiar velocity) which are called "siblings" (Brown 2014). Calculating distances using siblings can also help mitigate systematic uncertainties stemming from the host galaxy properties (Kelly et al. 2010; Sullivan et al. 2010; Lampeitl et al. 2010). Recent studies on SNe Ia siblings include four SNe in NGC1316 (Stritzinger et al. 2010), SN 2007on and SN 2011iv in NGC 1404 (Gall et al. 2018) and SN2013aa and SN 2017cbv in NGC 5643 (Burns et al. 2020).

Fakhouri et al. (2015) introduced the term "twin" supernovae. Twins are SNe that show analogous spectral features that imply parallel progenitor scenarios and explosion mechanisms. While Fakhouri et al. (2015) were able to significantly reduce absolute magnitude differences using twins, another study by Foley et al. (2020) found a significant difference in absolute magnitude for the two twins SN 2011by and SN 2011fe. Additionally, SN 2007on and SN 2011iv were also found to be inconsistent with each other despite being in the same galaxy (Gall et al. 2018). SN 1997cn (Turatto et al. 1998a) and SN 2015bo are spectrally similar fast-declining SNe in NGC 5490, and the existence of these two supernovae presents a rare opportunity to use the power of supernova siblings and twins to determine distances that do not suffer from a slew of systematic uncertainties.

In this paper, we present a detailed multi-wavelength analysis of the fast-declining SN 2015bo that is structured as follows: §2 presents the data used and a brief analysis of the host galaxy. Light and color curves are derived and compared to other SNe Ia in §3. Spectra are presented in §4 and compared to several samples of other sub-types of SNe and sub-luminous SNe. Doppler velocity measurements and pseudo-equivalent width calculations are also presented in §4. In §5, we determine the distance to SN 2015bo and compare it to the distance derived from the photometry of SN 1997cn: another fast-declining SN which exploded in the same host galaxy. Final discussion and concluding remarks are offered in §6. Throughout this work, phases are reported relative to rest-frame B-band maximum and given values are corrected for foreground galactic extinction.

2. DATA

SN 2015bo (a.k.a. PSNJ14095513+1731556) was discovered at $\alpha = 14^h09^m55^s.130$, $\delta = +17°31'55''.60$ by Howerton (2016) on 2015-02-14 at 10:37:06 UT. It was $m_V = 18.4$ mag at discovery.

There were two last non-detections; one from the Catalina Real-Time Transient Survey (CRTS; Drake et al. (2009) and the other from the All-Sky Automated Survey for SuperNovae (ASAS-SN; Shappee et al. 2014; Kochanek et al. 2017) on 2015-01-28T10:22:17 and 2015-02-08T13:47:20.40, respectively. Their respective magnitude limits were $m_V = 20.4$ and $m_g = 17.76$. SN 2015bo was classified as a 1991bg-like SNe Ia by the *Public ESO Spectroscopic Survey of Transient Objects* (PESSTO; Smartt et al. 2015) based on a spectrum taken on 2015-02-15 at 08:29:43 UT (Yaron 2017). It exploded in the type E galaxy NGC 5490 at a redshift of $z = 0.0161$[1]. The foreground Galactic extinction towards SN 2015bo is $E(B-V)_{mw} = 0.023$ mag (Schlafly & Finkbeiner 2011). Table 1 contains properties of both SN 1997cn and SN 2015bo, as well as their host galaxy.

Data for this work comes from two projects: the *Carnegie Supernova Project II* (CSP-II; Phillips et al. 2019) and PESSTO. CSP-II ran from 2011-2015 with the aim of obtaining high precision follow-up observations of SNe, mainly using telescopes at Las Campanas Observatory. PESSTO's objective was to obtain high quality spectral observations of transient sources using the New Technology Telescope (NTT) in La Silla.

2.1. *Photometric Observations*

Photometric observations were acquired in the $uBVgriJHY$ filters from -6.9 d to $+105.8$ d relative

[1] van den Bosch et al. (2015) from ned.ipac.caltech.edu.

Table 1. Properties of SN 1997cn, SN 2015bo and their host galaxy, NGC 5490.

Parameters	Value	Ref.
SN 2015bo:		
RA (J2000)	$14^h09^m55^s.13$	(1)
	212.47971 (deg)	(1)
Dec (J2000)	$+17°31'55''.60$	(1)
	17.53211 (deg)	(1)
$t(B)_{max}$ (JD)	2457078.3 ± 0.1 (d)	This work
M_B [a]	−17.50 ± 0.13 (mag)	This work
$E(B-V)_{MW}$	0.023 (mag)	(2)
$E(B-V)_{Host}$	0.00 ± 0.00 (mag)	This work
s_{BV} [b]	0.48 ± 0.01	This work
Δm_{15}(B) [c]	1.91 ± 0.01 (mag)	This work
SN 1997cn:		
RA (J2000)	$14^h09^m57^s.76$	(7)
	212.49067 (deg)	(7)
Dec (J2000)	$+17°33'32''.32$	(7)
	+17.54231 (deg)	(7)
$t(B)_{max}$ (JD)	2450588.3 ± 0.1 (d)	This work
M_B [e]	−17.43 (mag)	This work
$E(B-V)_{MW}$	0.023 (mag)	(2)
$E(B-V)_{Host}$	0.03 (mag)	(7)
s_{BV} [b]	0.35 ± 0.06	This work
Δm_{15}(B) [c]	1.90 ± 0.05 (mag)	(7)
NGC 5490:		
Type	Elliptical	(3)
RA (J2000)	$14^h09^m57^s.295$	(4)
	212.488728 (deg)	(4)
Dec (J2000)	$+17°32^m43^s.98$	(4)
	17.545551 (deg)	(4)
Velocity, v	12 km s^{-1}	(5)
z_{helio}	0.0161 ± 0.0001	(6)
μ [d]	34.21 ± 0.15 (mag)	(6)

References:(1) Howerton (2016); (2) Schlafly & Finkbeiner (2011); (3) de Vaucouleurs et al. (1991); (4) Adelman-McCarthy et al. (2008); (5) Simien & Prugniel (1997); (6) Kowalski et al. (2008); (7) Jha et al. (2006)

[a]Corrected only for both Galactic extinction using $R_V = 3.1$

[b]Obtained using a Gaussian process fit in SNooPY.

[c]Obtained using direct Gaussian process interpolation to the B-band.

[d]Corrected to the CMB rest frame and calculated using H_0=73 km s^{-1} Mpc^{-1}, Ω_m=0.27, and Ω_Λ=0.73, which is used throughout this work.

[e]This value is from light curve models fit to the data rather than directly from the data.

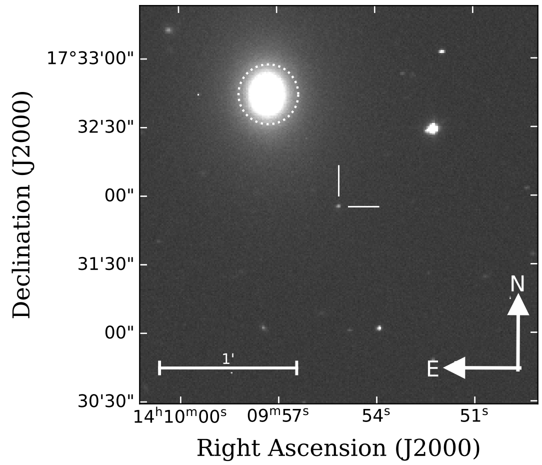

Figure 1. Finder chart for SN 2015bo using an image observed by the Swope Telescope in the i-band on 2015-04-19T08:56:55.

to rest-frame B-band maximum light. Optical photometry was obtained from the Swope telescope, and the near infrared (NIR) photometry came from the du Pont telescope. Both telescopes are located at the Las Campanas Observatory. All photometric observations are presented in the natural system and reduced using the methods described in Krisciunas et al. (2017) and Phillips et al. (2019). Logs of the optical and NIR observations are presented in Tables B1 and B2. Host-galaxy template subtraction was not required for SN 2015bo as it is located far away from the center of the host.

2.2. *Spectroscopic Observations*

Sixteen optical and one NIR spectra of SN 2015bo were obtained from −7.8 d to +31.8 d relative to rest-frame B-band maximum light. Spectra were taken on a variety of instruments including SPRAT mounted on the Liverpool Telescope, ALFOSC on the Nordic Optical Telescope, EFOSC on the New Technology Telescope, and WFCCD on the du Pont telescope. The optical spectra were reduced using the standard IRAF[2] packages and methods described in Hamuy et al. (2006); Folatelli et al. (2013); Smartt et al. (2015). The NIR spectrum was obtained with the Folded-port InfraRed Echellette (FIRE) on the Baade telescope at the Magellan observatory and reduced using the methods described in Hsiao et al. (2019). Table 3 presents a summary of the spectral data.

[2] The Image Reduction and Analysis Facility (IRAF) is distributed by the National Optical Astronomy Observatory, which is operated by the Association of Universities for Research in Astronomy, Inc., under cooperative agreement with the National Science Foundation.

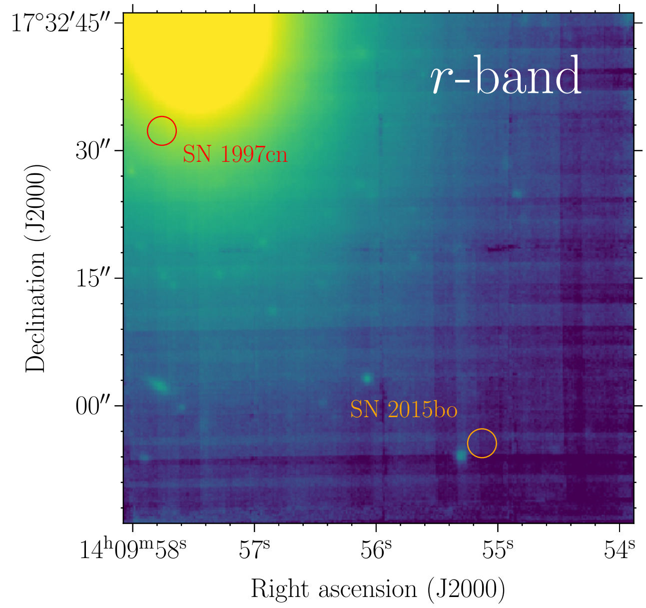

Figure 2. The MUSE data-cube synthetic r-band image. The image was obtained by convoluting the spectra by a r filter transmission. The orange and red circles represent a one square kpc aperture centered on the positions of SN 2015bo and SN 1997cn, respectively.

2.3. *Host Galaxy*

Integral-field spectroscopy of NGC 5490 was obtained on 2021-01-27 08:04:06, with the Multi-Unit Spectroscopic Explorer (MUSE; Bacon et al. 2010). MUSE is mounted on the Unit 4 telescope at the ESO Very Large Telescope at the the Cerro Paranal Observatory. These host observations were obtained as part of the All-weather MUSE Supernova Integral-field Nearby Galaxies (AMUSING; Galbany et al. 2016; López-Cobá et al. 2020) survey. AMUSING is an ongoing project that analyzes the host galaxies of SNe to study their environments.

Figure 2 presents a synthetic r-band image extracted from MUSE observations of the host galaxy. SN 2015bo is distant from the center of the host galaxy, NGC 5490. This suggests that host galaxy extinction is minimal for SN 2015bo. The object adjacent to SN 2015bo is an unrelated background galaxy.

3. PHOTOMETRY

3.1. *Light Curves*

The multi-band $uBVgriJHY$ light curves are presented in Figure 3. The filters are organized top-down from blue wavelengths to red wavelengths. Data from the five optical filters ($BVgri$) extend to $\sim$+80 d after the time of B-band maximum ($\mathrm{t}(B)_{\mathrm{max}}$). BVg rise on time scales longer than $\sim$10 d, but the true time of explosion is uncertain as the last non-detections are not constraining.

To derive important photometric quantities such as $\mathrm{t}(B)_{\mathrm{max}}$, maximum m_B, and $\Delta\mathrm{m}_{15}(\mathrm{B})$, we utilize the SuperNovae in object-oriented Python (SNooPy; Burns et al. 2011, 2014) fitting program. The B-band was interpolated using a Gaussian process technique which underwent 150 Monte Carlo iterations to determine the uncertainties. The 1-σ deviation from the Monte Carlo iterations was used as the uncertainty for the derived values. We used the 1991bg-like SN spectral energy distribution (SED) template within SNooPy[3] to perform K-corrections. This correction template is used throughout this work for fitting fast decliners with SNooPy. Values of $\mathrm{t}(B)_{\mathrm{max}} = 2457078.3 \pm 0.1$ d and maximum $\mathrm{m}_B = 16.83 \pm 0.01$ mag were computed. $\Delta\mathrm{m}_{15}(\mathrm{B})$ and s_{BV} were calculated using the same direct Gaussian process interpolation technique. For s_{BV}, only data with both B- and V-band taken on the same night were used. The values of $\Delta\mathrm{m}_{15}(\mathrm{B})$ and s_{BV} are 1.91 ± 0.01 mag and 0.48 ± 0.01, respectively. A table of derived maximum apparent magnitudes in each CSP filter is presented in Table 2.

The multi-band light curves were fit with the 1991bg-like template and the EBV2 model in SNooPy to determine the host-galaxy extinction and to derive a SN dependent distance modulus to the host galaxy. A host-galaxy extinction of $E(B-V)_{host} = 0.21 \pm 0.07$ mag, and a distance modulus of $\mu = 34.36 \pm 0.01$ (stat) $\pm$ 0.11 (sys) mag were obtained. However, no Na I lines were seen in the spectra, so this extinction term from SNooPY is most likely inaccurate. Additionally, SN 2015bo is far away from its elliptical host galaxy, reducing the chance of significant host-galaxy extinction. We conclude that SN 2015bo does not suffer from much, if any, host-galaxy extinction. This is confirmed by deriving an upper limit on Na I as described in Ashall et al. (2021), which is converted to a limit on $E(B-V)$ via the method of Poznanski et al. (2012). This limit is 0.02 mag – which is lower than the value calculated by SNooPy. We conclude that the host-galaxy extinction must be minimal. However, the host galaxy extinction derived from SNooPy is used by SNooPy when it derives the distance modulus. This means extra care must be taken when working with any SNooPy fits that could be influenced by its derived host-galaxy extinction. Further discussion about distance calculations and a more accurate derivation of the distance modulus and its systematic uncertainty can be

[3] Taken from https://c3.lbl.gov/nugent/nugent_templates.html.

Table 2. Table of maximum light apparent magnitudes

Filter CSP-II	Magnitude [mag]	Uncertainty [mag]
u	18.15	0.01
V	16.84	0.01
B	16.44	0.01
g	16.62	0.01
r	16.27	0.01
i	16.62	0.01
H[a]	16.51	0.04

[a]the H-band was the only NIR band where SNooPy was able to derive a maximum value. This is likely due to the lack of data in the NIR regime.

found in §5. Finally, the SNooPy fits (see Figure 4) show that SN 2015bo's photometry is well matched by 1991bg-like SNe light-curve templates.

Figure 5 compares the light curves of SN 2015bo in $BVgri$ with a selection of sub-types of SNe Ia from CSP-II. SN 2015bo's light curve resembles 1991bg-like SNe, and it evolves more quickly than the other types of SNe Ia in every band. The lack of a distinctive knee-type feature in the r-band when compared to normal and 1991T-like SNe highlights this difference. The i-band can be used to confirm if a SN is a sub-luminous SN. SN 2015bo, like many other sub-luminous SNe, lacks a secondary i-band maximum, whereas normal and 1991T-like SNe have a distinct secondary maximum. In normal SNe Ia, the secondary i-band maximum comes from recombination of iron group elements (Höflich et al. 2002; Kasen 2006; Jack et al. 2015), however, in 1991bg-like SNe, Kasen (2006) and Blondin et al. (2015) propose the recombination either does not occur or occurs earlier which causes the maxima to merge and appear as one maximum in the light curve. This is also why the i-band peak occurs after B-band maximum. The importance of the second i-band maximum for using SNe Ia as distance indicators is discussed in §5. The i-band for SN 2015bo is also slightly broader than the 1991bg-like SNe comparison sample. Interestingly, SN 2015bo shows some similarities with 2002cx-like SNe in the Bgr bands, but SN 2015bo declines significantly faster than 2002cx-like SNe in the Vi bands. Although 2003fg-like SNe show a somewhat wider variety in their light curve morphologies, it is still evident that SN 2015bo declines more quickly than all 2003fg-like SNe in all plotted filters, and for most 2003fg-like SNe this difference in decline rate is significant.

Ashall et al. (2020) showed SNe Ia can be photometrically sub-typed by just their s_{BV} value and their time of primary i-band maximum relative to B-band maximum (t^{i-B}_{max}). Figure 6 presents this relationship with SN 2015bo overlaid. SN 2015bo is located in the 1991bg-like SNe area of the parameter space where there are fewer SNe. This suggests the classification that SN 2015bo is a 1991bg-like SN.

3.2. *Color Curves*

In Figure 7, the color curves of SN 2015bo are presented. Color curves are obtained by subtracting photometric points observed on the same night. No interpolations between data points were performed. At early times, the color is a diagnostic of the temperature of the photosphere, so Figure 7 provides an approximate measurement of the temperature over time. Both the $B-V$ and the $g-r$ color curves are similar; they exhibit sharp increases from bluer to redder from ∼0 d to ∼+15 d and then turn to become bluer after ∼+15 d, however, $g-r$ declines more quickly than $B-V$ over this time frame. After ∼+55 d, the photosphere is well within the ejecta and the color no longer measures the temperature, but rather differences in ionization state from a mixture of absorption and emission features. At later epochs, $B-V$ flattens off to eventually reach a value of ∼0.5 mag at ∼+80 d, whereas $g-r$ continues to decline as far out as ∼+100 d to reach a value of ~ -0.4 mag. The $V-r$ color curve also peaks near $/sim$+15 d, but it does not rise as steeply as $B-V$ or $g-r$. When it declines, $V-r$ is broader than $g-r$ and is approximately the same slope as $B-V$. The $r-i$ color curve displays a slightly later red peak at around +20 d rather than around +15 d, and it also has a noticeably less steep increase. It also flattens off over time rather than decline. The flattening starts at ∼+30 d, which is earlier than when the $B-V$ color curve may start to flatten in the last two $B-V$ data points. These color curve shapes are strange; they may provide a potential explanation to why SNooPy wants to have a redder extinction than is realistic.

Figure 8 compares the color curves of SN 2015bo to a variety of other SNe Ia. The comparison SNe Ia are corrected for both their respective galactic and host-galaxy extinctions. SN 2015bo is plotted in black diamonds, with two transitional SNe Ia, SN 2007on and SN 2011iv, plotted in blue circles and red squares, respectively. These two transitional objects are plotted individually because they also exhibit the same peculiar blue rise in the $r-i$ color curve that SN 2015bo has

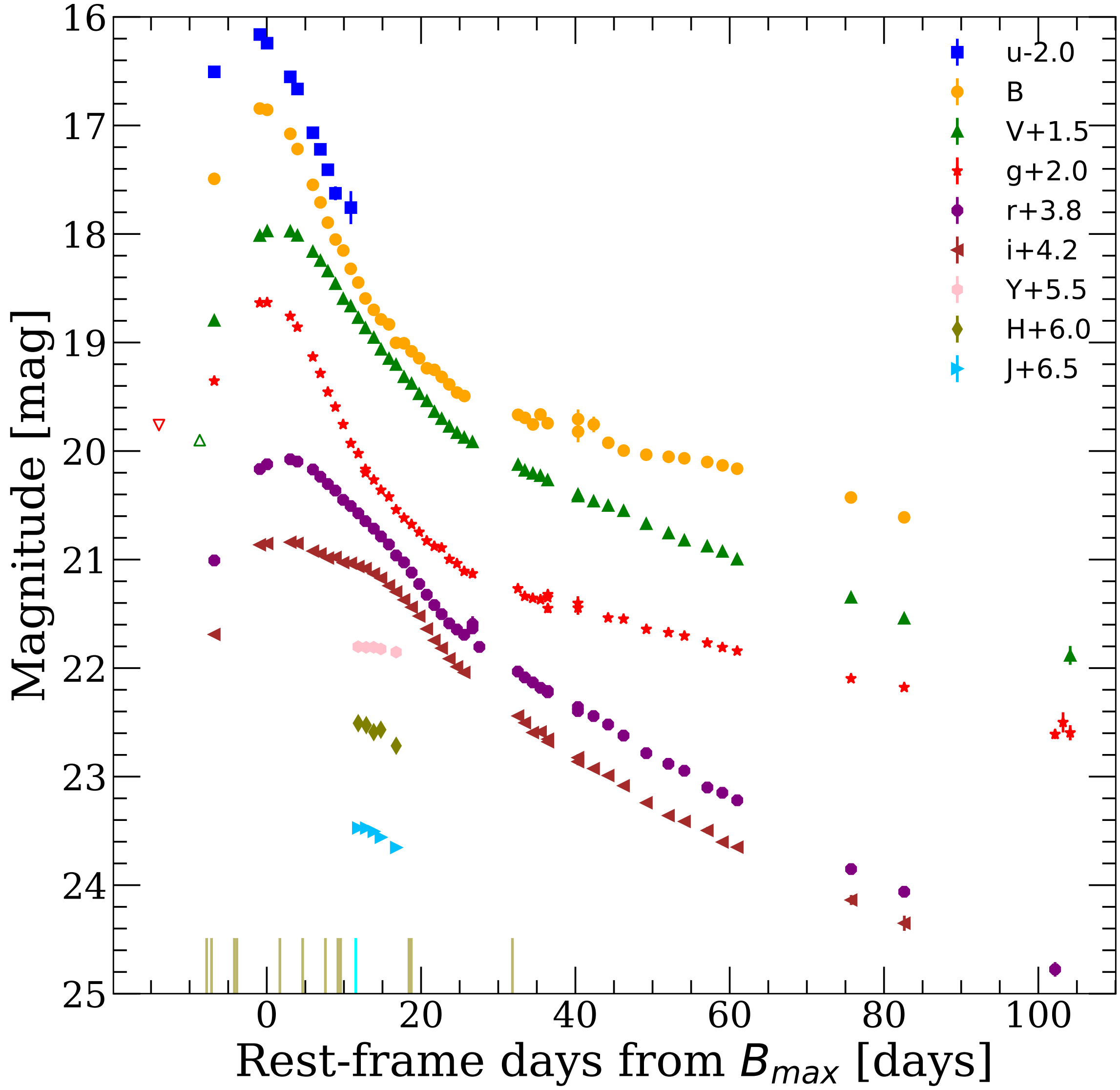

Figure 3. Rest-frame optical and NIR photometry of SN 2015bo. The V-band discovery point is given as a green upward open triangle. The last-non detection from ASAS-SN in the g-band is provided as a red downward open triangle. Dark khaki lines on the bottom horizontal axis represent epochs with optical spectra, and the cyan line represents the epoch of our NIR spectrum.

after $\sim$+40 d (see below for details). SN 2007on and SN 2011iv are interesting objects in their own right; they both exploded in NGC 1404, and they are both transitional SNe Ia. Detailed discussions of SN 2007on and SN 2011iv can be found in Gall et al. (2018) and Ashall et al. (2018).

In $B - V$, SN 2015bo starts bluer than the comparison sample and becomes more red that the comparison sample over time after $\sim$+30 d. Its Lira tail (the region in the $B - V$ color curve after $\sim$+20 d for which the majority of SNe have similar slopes; Phillips et al. 1999) is the steepest of our sample. Comparing SN 2007on and SN 2011iv, Gall et al. (2018) found SN 2011iv was bluer earlier on, yet it became redder than SN 2007on at $\sim$+30 days. Gall et al. (2018) interpreted this as an effect from the progenitor white dwarfs having differing central densities at the time of explosion. Therefore, the ^{56}Ni distributions would be different for SN 2007on and SN 2011iv. At B-band maximum and at the reddest color inflection point, SN 2015bo has a similar $B - V$ color to SN 2007on; however, the slope of the decline in the Lira tail is steeper in SN 2015bo than both SN 2007on and SN 2011iv. This could be an indication that the central density of SN 2015bo is even lower than SN 2007on.

The $V - r$ color curve for SN 2015bo is unique. It reaches a red peak higher than any other observed SN Ia in our comparison sample. This is peculiar, especially

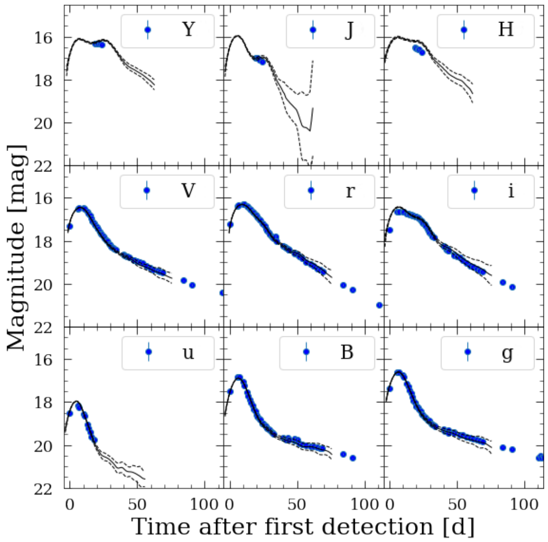

Figure 4. SNooPy fits described in §3.1. The vertical axis is plotted in magnitudes, and the horizontal axis is in days after the first data point.

considering this same behavior does not occur in either $r-i$ or $B-V$ colors, or with other transitional or 1991bg-like SNe. Additionally, it seems that the triumvirate of SN 2007on, SN 2011iv, and SN 2015bo decline in $V-r$ more rapidly than normal SNe Ia after $\sim$+50 d past t$(B)_{\mathrm{max}}$.

Another intriguing property of SN 2007on, SN 2011iv, and SN 2015bo is the redward rise of the $r-i$ color curve at $\sim$+40 d after B-band maximum. This red color shift could be due to the fact that fast decliners are [Ca II] strong. Therefore the [Ca II] $\lambda\lambda$ 7291.5, 7323.9 emission, which is usually seen beginning at $\sim$+40 d (Taubenberger 2017), will affect the $r-i$ color curve. This difference in the $r-i$ color curve after $\sim$+40 d could provide a robust way to photometrically distinguish a subset of transitional and/or 1991bg-like SNe that may share a progenitor scenario or explosion mechanism or to distinguish fast-declining SNe from normal SNe Ia.

The $r-i$ color minimum that occurs just after t$(B)_{\mathrm{max}}$ for SN 2007on, SN 2011iv, and SN 2015bo are also significantly earlier and bluer than normal SNe Ia. This earlier first turning point could provide a good way to identify sub-luminous SNe Ia in future studies. We see no evidence for an inflection point at $\sim$0-10 d in the $V-r$ color despite having data during the epochs where all other SNe Ia in the sample turn.

3.3. *Luminosity-Width Relation*

The peak absolute magnitude of SN 2015bo is calculated from the light curves to be $M_B = -17.50 \pm 0.13$ mag. This value has been corrected for only foreground extinction only and uses the Cosmic Microwave Background (CMB) corrected distance modulus. This distance modulus is 34.21 ± 0.15 mag, and it was derived from a standard cosmology with H_0=73 km s^{-1} Mpc^{-1}, Ω_m=0.27 and Ω_Λ=0.73, which is used throughout this work.

The luminosity-width relation is plotted in Figure 9 using comparison SNe from the CSP. SN 2015bo is plotted without corrections for host extinction (since host galaxy extinction is most likely negligible for SN 2015bo) and the rest of the sample is corrected for host galaxy extinction. The left side of the figure is for the B-band, whereas the right side of the figure is for the V-band. SN 2015bo is located with the transitional and 1991bg-like SNe and is within the area of parameter space of $s_{BV}\approx$0.5, where there is a lack of objects (Ashall et al. 2016). The left panels of the figure use absolute magnitude values from SNooPy template fits; the right panels use M_V and Δm_{15}(V) from direct Gaussian process fits with the same method as in §3.1. This is the reason there is less scatter in the B-band compared to the V-band. Only SNe passing quality cuts are plotted on the right side of the plot. These cuts were made to eliminate poorly measured comparison SNe or objects that suffered from significant extinction and/or uncertain distances due to peculiar velocities.

In the top left panel, SN 2015bo is located in the degenerate region of the parameter space. The reason for this degeneracy is discussed in detail in Burns et al. (2014). However, when the correlations are plotted as a function of s_{BV}, SN 2015bo occupies the bright end of the 1991bg-like SNe parameter space. In the B-band, M_B is among the parameter space occupied by other fast decliners. In the V-band, SN 2015bo is in the fast-declining, under-luminous parameter space as well.

SN 1997cn is also plotted in Figure 9 using the photometry from Jha et al. (2006). Due to the photometry starting well after maximum in all bands, we were unable to directly calculate the time of B- or V-band maxima, maximum magnitudes in B- and V-bands, Δm_{15}(B), Δm_{15}(V), or s_{BV}. Because of this, values from the best-fit templates derived from the SNooPy EBV2 model were used for SN 1997cn. In all panels, SN 1997cn occupies the same parameter space as SN 2015bo.

3.4. *Bolometric Light Curves*

Pseudo-bolometric light curves were constructed using the direct spectral energy distribution method within SNooPy. The wavelength range was from 3,000 Å to 19,370 Å. In short, the method converts the magnitudes into fluxes to produce an SED, the 1991bg-like spectral templates are used for k- and S-corrections, and the SED is integrated and scaled with respect to the

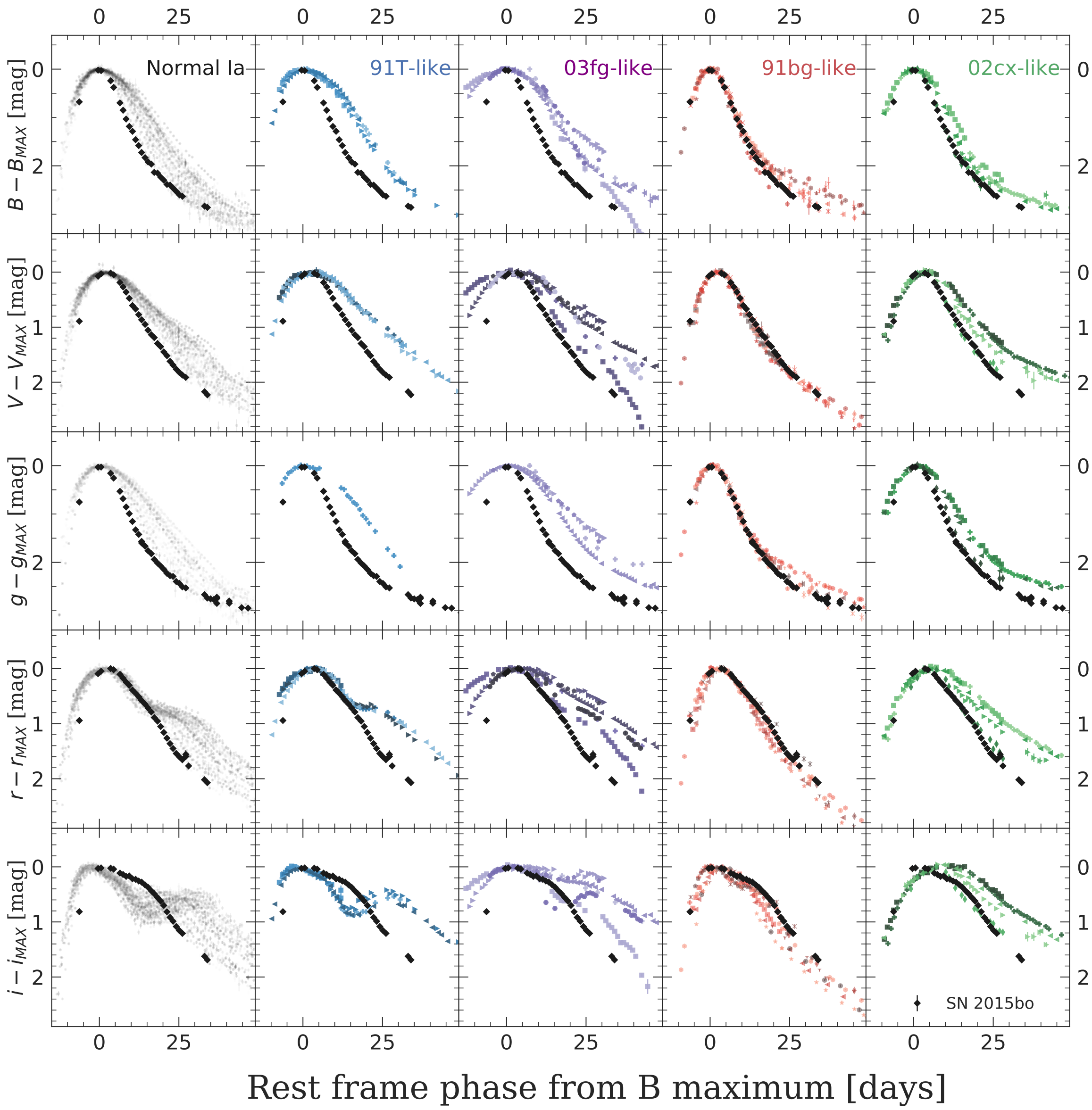

Figure 5. The B-band (first row), V-band (second row), g-band (third row), r-band (fourth row), and i-band (fifth row) light curves compared to a selection of SNe Ia sub-types: normal (first column/grey), 91T-like (second column/blue), 03fg-like (third column/purple), 91bg-like (fourth column/orange), and 02cx-like (fifth column/green). SN 2015bo (black points) deviates significantly from all other types of SNe Ia, but matches quite well with other 1991bg-like SNe. Comparison SNe are from Ashall et al. (2020).

distance modulus to produce a bolometric flux at each epoch. Due to the lack of temporal coverage in the infrared data, we use a Rayleigh-Jeans model to extrapolate our SEDs when data was not available. The SEDs were also corrected for Milky Way extinction. The error on the bolometric light curve was determined via varying the distance modulus through 100 Monte Carlo iterations. To do this, the distance modulus was treated as a Gaussian distribution. A Gaussian process was used to determine the maximum for each iteration. The mean value of these maxima from the Monte Carlo iterations was taken as the final peak pseudo-bolometric luminosity and the mean of the standard deviations of the maxima was taken as the uncertainty.

The peak pseudo-bolometric luminosity of SN 2015bo is $L_{bolo}^{peak} = 0.33 \pm 0.03 \times 10^{43}$ erg s^{-1}. Using the relation between L_{bolo}^{peak} and ^{56}Ni mass presented in Stritzinger et al. (2006) and Arnett (1982), a ^{56}Ni mass of $0.17 \pm 0.05 M_{\odot}$ was derived. Calculated values are compared to other SNe Ia presented in Ashall et al. (2018) in Figure 10. Both the bolometric luminosity and ^{56}Ni mass of SN 2015bo are consistent with the general

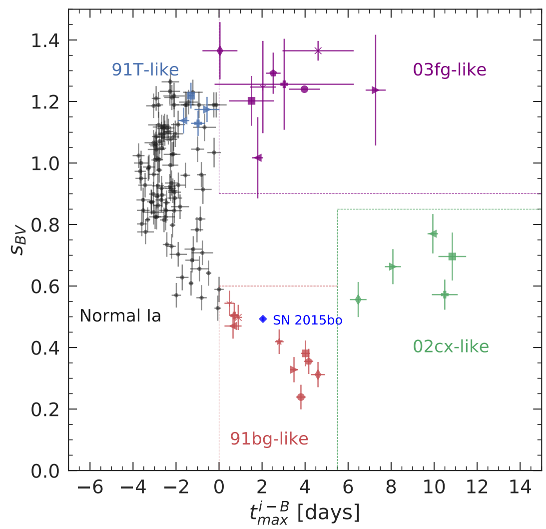

Figure 6. The color stretch parameter s_{BV} as a function of time difference between i- and B-band maxima, t_{max}^{i-B}. Different sub-types of SNe Ia occupy different areas of the plot, as shown in Ashall et al. (2020).

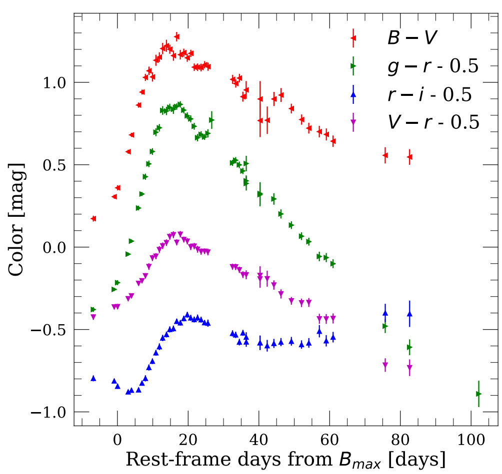

Figure 7. Color versus rest-frame days from B_{max}. From top to bottom, plotted colors are $B-V$ (red), $g-r$ (green), $V-r$ (magenta), and $r-i$ (blue). Color curves have been corrected for Milky Way, but not host-galaxy, extinction.

trend presented in Ashall et al. (2019a). SN 2015bo has a lower luminosity and lower ^{56}Ni mass than the majority of the CSP comparison sample. This places it near other 1991bg-like SNe.

A similar pseudo-bolometric light curve and nickel mass were not computed for SN 1997cn because the data for SN 1997cn is insufficient to directly derive a nickel mass. However, Turatto et al. (1998a) found a ^{56}Ni mass of $\sim 0.1 M_\odot$for SN 1997cn using models.

4. SPECTRA

Photometry is a powerful tool for classifying and studying supernovae, but it does not reveal the full picture. Spectroscopic observations complement photometric ones and enable further understanding of the elemental composition of SNe. Due to the homologous ($v = rt$) expansion of a SN ejecta ~10 s after the explosion, obtaining a time series of spectra allows the reconstruction of the evolution of the ejecta over time. In addition to providing composition information, spectra also can be used to derive velocities of the ejecta and provide additional information on the physics of the explosion such as the temperature, the ionization state, and the kinetic energy.

4.1. *Optical Spectra*

Figure 11 presents a time series of the optical spectra compiled here for SN 2015bo. The spectra span from −7.8 d to +31.8 d relative to B-band maximum. The spectra are dominated by features of intermediate-mass and Fe-group elements as well as oxygen. The main spectral features we identify are: Ca II H&K $\lambda\lambda$ 3968, 3933, Ti II λ 4395, Fe II $\lambda\lambda$ 4923, 5169, Fe III λ 5156, S II $\lambda\lambda$ 5449, 5623, Si II $\lambda\lambda$ 5972, 6355, O I λ 7774, and Ca II $\lambda\lambda$ 8498, 8542, 8662 NIR lines. These lines are identified based on Ashall et al. (2016) and Mazzali et al. (1997).

Spectra of SN 2015bo are compared to other sub-types of SNe Ia at maximum light and +20 d in Figure 12. All objects in the sample are dominated by intermediate-mass elements and Fe-group elements. Most have a strong Si II λ 6355 feature. SN 2015bo is most similar to SN 1991bg, as demonstrated by the strong Si II λ 5972 feature. In other SNe, the Si II λ 5972 feature is weak or entirely absent (e.g. SN 1991T and SN 2011fe). While not as strong as SN 1991bg, SN 2015bo's Ti II λ 4400 feature is still present. This feature (Ti II λ 4400) is only observed in our sample in SN 2015bo, SN 1991bg and SN 2006bt. As the strength of the Si II λ 5972 and Ti II λ 4400 is indicative of temperature, this suggests SN 2015bo has a photospheric temperature between those of SN 1991bg and a normal Ia such as SN 2011fe. By +20 d, all of the SNe in the sample look similar because the photosphere is well within the ^{56}Ni region.

Figure 13 compares SN 2015bo to other SN 1991bg-like and transitional SNe Ia. The sample is arranged by s_{BV} value; there is a trend that SNe with smaller s_{BV} have stronger Si II λ 5972 features. The Ti II λ 4400 feature also shows the same relationship between depth and s_{BV}. Within this trend, SN 2015bo is located between SN 2005bl and SN 1986G both in terms of s_{BV} and strength of the Ti II λ 4400 and Si II λ 5972 features.

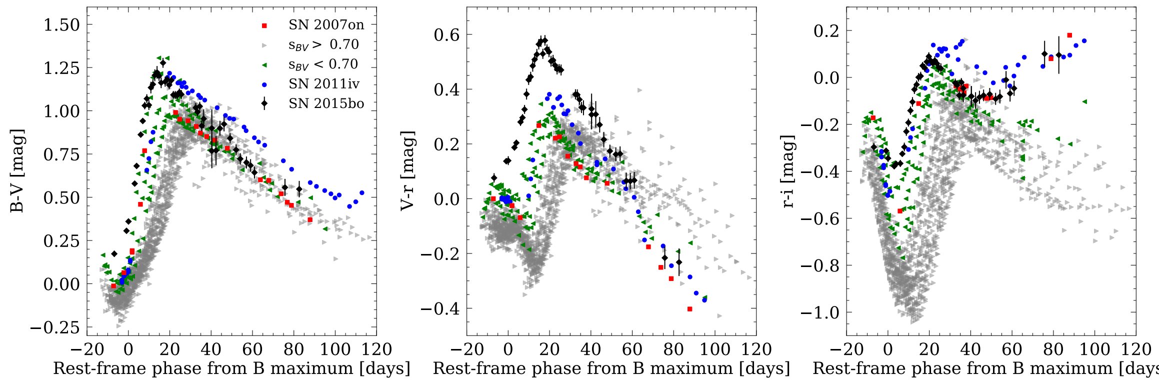

Figure 8. Comparison of color curves for SN 2015bo and other SNe. Plotted colors from left to right are $B-V$, $V-r$, and $r-i$. SN 2015bo is plotted in black diamonds with two similar SNe Ia, SN 2007on and SN 2011iv, plotted in blue circles and red squares, respectively. Green, left-facing triangles are other fast decliners; the condition $s_{BV} < 0.70$ effectively segregates between normal and fast-declining SNe Ia. Grey, right-facing triangles are all other types of SNe Ia. All comparison SNe Ia data points have been corrected for both Milky Way and host-galaxy extinction, whereas SN 2015bo is only corrected for galactic extinction since there is most likely an insignificant amount of host-galaxy extinction.

Table 3. Log of spectroscopic observations.

UT Data	MJD [days]	Epoch [a] [days]	Telescope	Spectrograph
2015-02-15	57068.35	−7.8	NTT[b]	EFOSC2
2015-02-16	57069.00	−7.2	LT[c]	SPRAT
2015-02-19	57072.00	−4.2	LT	SPRAT
2015-02-19	57072.34	−3.9	NTT	EFOSC2
2015-02-19	57072.36	−3.9	NTT	EFOSC2
2015-02-25	57078.00	1.7	DUP[d]	WFCCD
2015-02-28	57081.00	4.7	LT	SPRAT
2015-03-03	57084.00	7.6	LT	SPRAT
2015-03-03	57085.64	9.2	NOT[e]	ALFOSC
2015-03-05	57086.00	9.6	LT	SPRAT
2015-03-07	57088.00	11.5	Magellan	FIRE
2015-03-10	57092.69	16.2	NOT	ALFOSC
2015-03-14	57095.00	18.4	LT	SPRAT
2015-03-14	57095.30	18.7	NTT	EFOSC2
2015-03-14	57095.32	18.8	NTT	EFOSC2
2015-03-26	57108.63	31.8	NOT	ALFOSC

[a]Epoch phase relative to rest frame B-band maximum.
[b]New Technology Telescope.
[c]Liverpool Telescope.
[d]du Pont Telescope.
[e]Nordic Optical Telescope.

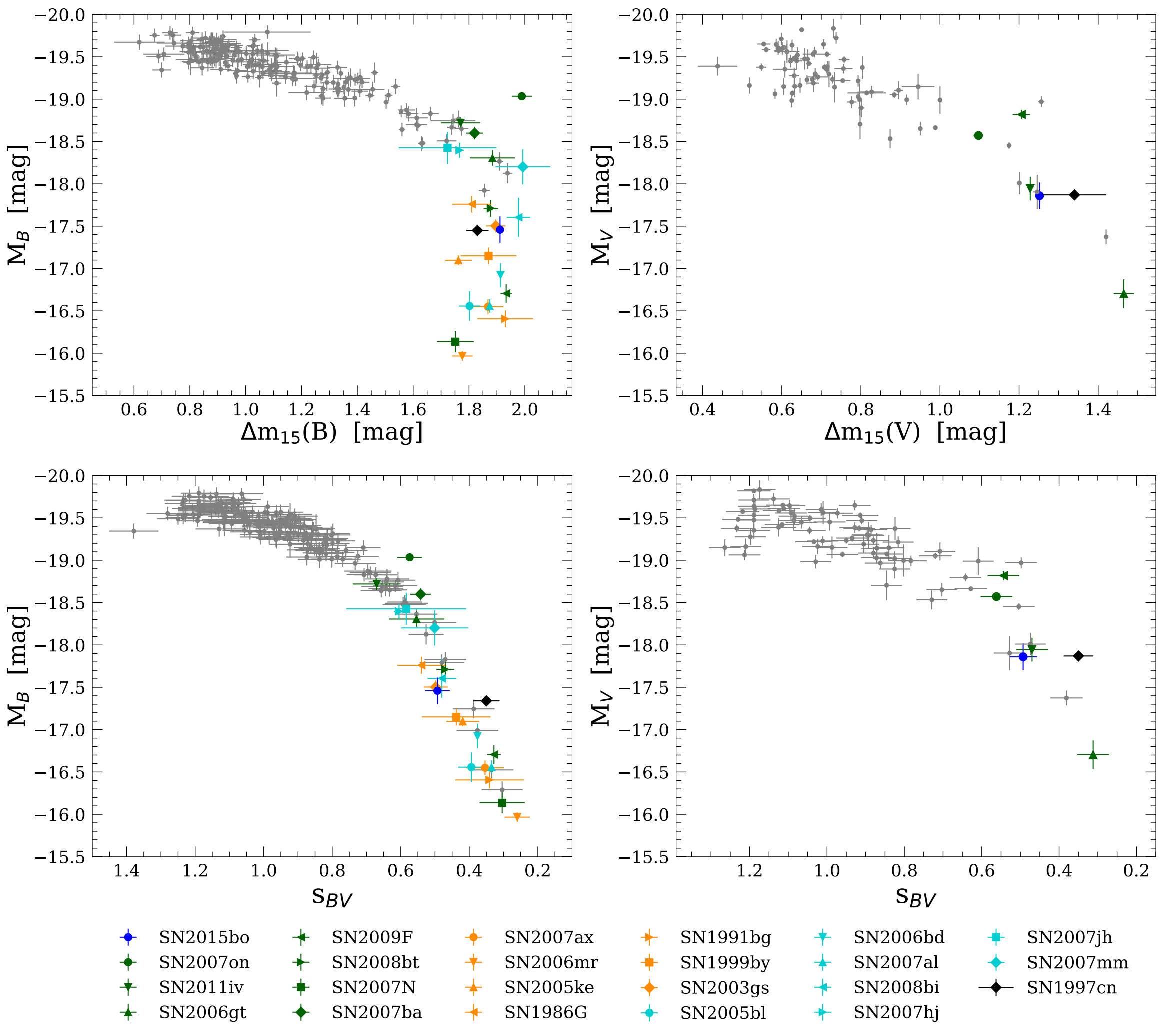

Figure 9. Luminosity-width relation using s$_{BV}$, Δm$_{15}$(B), and Δm$_{15}$(V). For all panels, the blue point is SN 2015bo. Other fast decliners are plotted as green, orange, or cyan diamonds, triangles, squares. SN 1997cn is plotted as the black diamond. Grey points are a sample of other sub-types and normal SNe Ia. *Top-Left*: Absolute B-band magnitude plotted against $\Delta m15(B)$. *Bottom-Left*: Absolute B-band magnitude plotted against s$_{BV}$. *Top-Right*: Absolute V-band magnitude plotted against $\Delta m15(V)$. *Bottom-Right*: Absolute V-band magnitude plotted against s$_{BV}$. For the left-hand side, s$_{BV}$ and Δm$_{15}$(B) values come from models within SNooPy, whereas on the right hand side s$_{BV}$ and Δm$_{15}$(V) are directly computed by SNooPy on the specific band. All background SNe that were calculated in SNooPy satisfy the following: $z > 0.01$, $A_V < 0.75$ mag, $\sigma M_V < 0.3$ mag, $\sigma\Delta\mathrm{m}_{15}(\mathrm{V}) < 0.05$ mag, and $\sigma s_{BV} < 0.05$. These choices were made to eliminate poorly measured background SNe or objects that suffered from significant extinction and/or uncertain distances due to peculiar velocities.

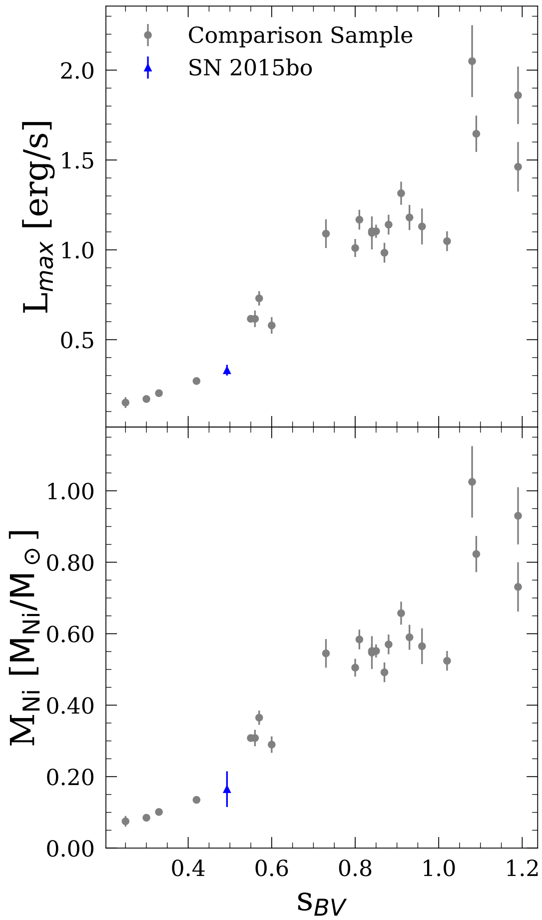

Figure 10. Pseudo-bolometric luminosity (top) and nickel mass (bottom) as a function of s_{BV}. SN 1997cn is plotted as the red, upward-facing triangle, SN 2015bo is plotted as the blue, downward-facing triangle, while other SNe Ia are grey circles.

Figures 9 and 10 confirm this; in both plots, SN 2015bo resides on the more luminous end of the fast decliners. These photometric results are consistent with spectral observations. SN 1997cn is also plotted to compare its spectra to the other SNe – it falls between SN 2005bl and SN 1991bg based on s_{BV} value.

Discussing spectral differences in a qualitative manner is helpful to see general trends, however, as a scientific method it is imprecise. Therefore, velocities and pseudo-equivalent widths are derived to provide a quantitative picture of SN 2015bo and its spectral relationship to other SNe Ia. These measurements are presented in §4.3.

4.2. *Velocity and pEW Fitting Method*

We fit all optical spectra using the Measure Intricate Spectral Features In Transient Spectra[4] (mistfits; S. Holmbo et al., in prep.) fitting program. This program was used to calculate both the wavelengths of each spectral feature and the pseudo equivalent-widths (pEW). To fit the wavelengths, spectra were smoothed using misfits' low-pass fast Fourier transformed filter spectra following the method described in Marion et al. (2009). An uncertainty spectrum was computed from the difference between the observed and smoothed spectra. The absolute values of the residuals were smoothed using a Gaussian filter where the smoothed residuals contain 68% of the absolute value of the residual level. This is used as the 1-σ error spectrum.

From there, a Gaussian function and a linear continuum were simultaneously fitted to each feature using the *velocity.gaussians* function within misfits. The initial guess continuum boundary points were selected by hand, and the best fit was determined by χ^2 minimization. A final wavelength and uncertainty were respectively determined using the mean and standard deviation of 1000 Monte Carlo iterations. This uncertainty was added in quadrature with the uncertainty of the instrument resolution to arrive at the final wavelength uncertainty. The relativistic Doppler formula and rest wavelength of the feature were used to convert the wavelength of the absorption minimum into velocities.

Pseudo-Equivalent Width determination followed the procedure presented in Garavini et al. (2007) using misfits' *width.shallowpew* function. The mean and standard deviation of 1000 Monte Carlo iterations were used as the pEW value and 1-σ uncertainty.

4.3. *Branch Diagram, Velocities, and pEW*

4.3.1. *Branch Diagram*

An additional way to classify SNe Ia into sub-types is to plot the pEW of Si II λ 5972 against Si II λ 6355 at maximum (Branch et al. 2006). Figure 14 shows SN 2015bo along with other SNe Ia. There are four regions: Shallow Silicon, Core Normal, Cool, and Broad Line. Core Normal SNe are a highly homogeneous group with similar spectral features. Broad Line SNe are similar to Core Normal, but have broader features. Likewise, Shallow Silicon are also similar to Core Normal but tend to have equally weak Si II λ 5972 and Si II λ 6355 features. Shallow Silicon SNe tend to be over-luminous. Finally, there are the Cool SNe. These objects are sub-luminous – strong Si II λ 5972 values are predominantly seen in sub-luminous SNe. SN 2015bo occupies the upper right area of the Cool region among other fast-declining, sub-luminous SNe Ia, whereas SN 1997cn falls in the upper central area of the Cool region.

4.3.2. *Velocities*

[4] https://github.com/sholmbo/misfits.

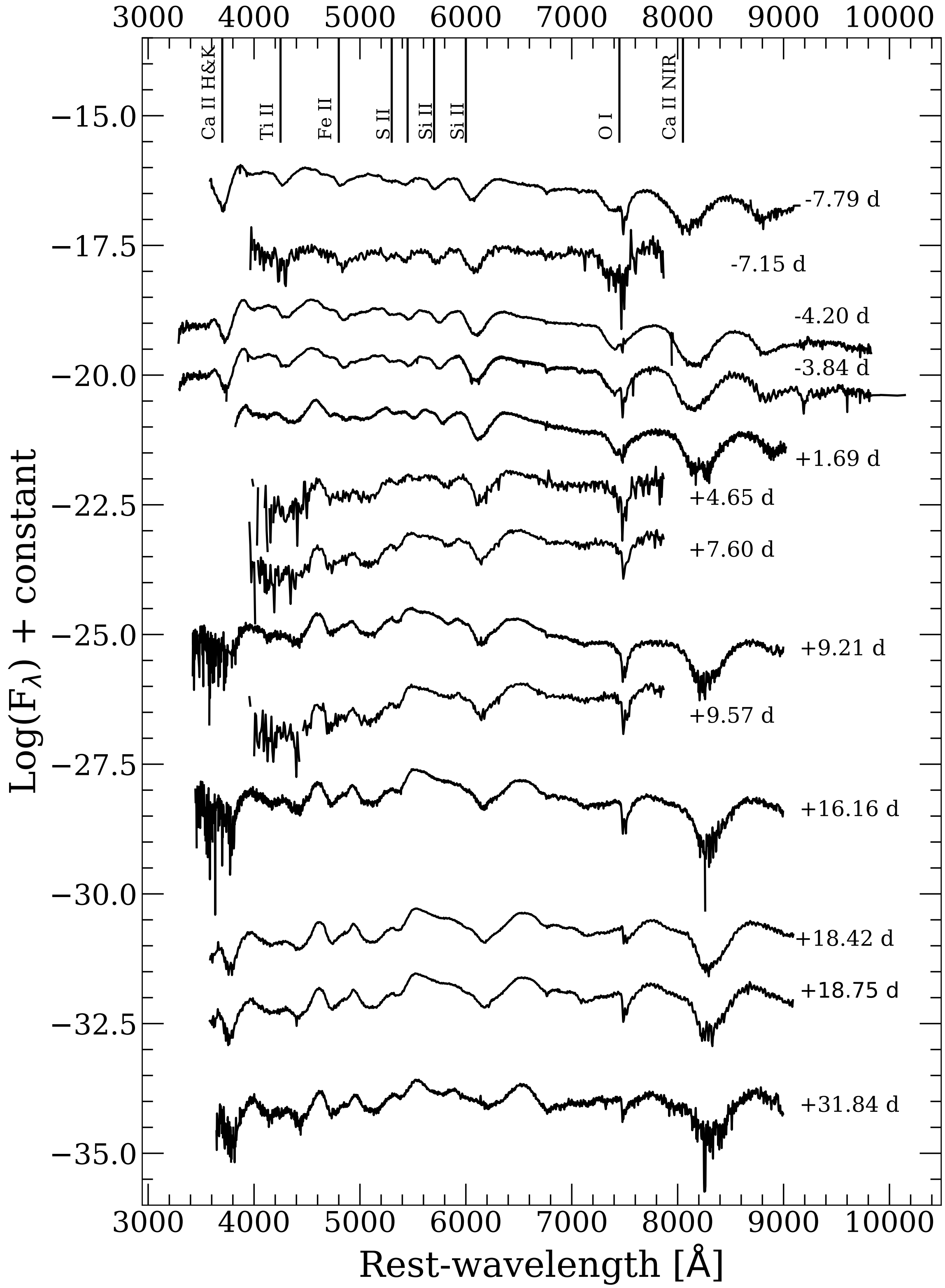

Figure 11. Time series of optical spectra for SN 2015bo. Times relative to rest-frame B-band maximum are provided next to each spectrum.

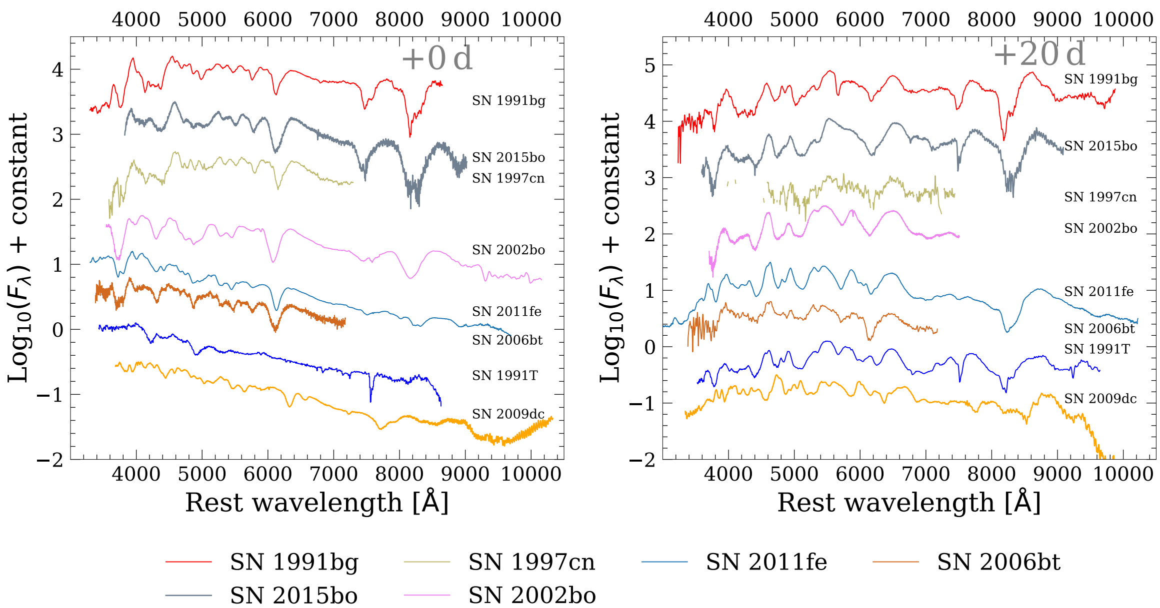

Figure 12. Comparison of SN 2015bo (grey) to other SNe Ia: SN 1991bg (Filippenko et al. 1992b); normal SNe Ia SN 2002bo (Benetti et al. 2004; Szabó et al. 2003) and SN 2011fe (Nugent et al. 2011); peculiar SN 2006bt (Foley et al. 2010b); the over-luminous SN 1991T (Phillips et al. 1992; Filippenko et al. 1992a); and the SN 2003fg-like SN 2009dc (Yamanaka et al. 2009). *Left*: Comparison at B-band maximum. *Right*: Comparison at +20 d from B-band maximum.

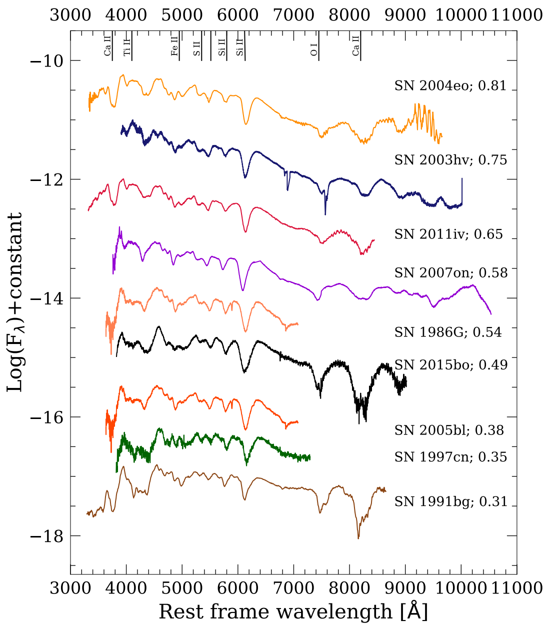

Figure 13. Comparison of optical spectra at the time of maximum B-band magnitude of 1991bg-like and transitional SNe Ia. From blue to red, the significant features are Ca II H&K $\lambda\lambda$ 3968, 3933, Ti II λ 4400, Fe II $\lambda\lambda$ 4923, 5169, S II $\lambda\lambda$ 5449, 5623, Si II $\lambda\lambda$ 5972, 635, O I λ 7774, and Ca II $\lambda\lambda$ 8498, 8542, 8662. s_{BV} values are taken from Ashall et al. (2018) Table 5, except for SN 1991bg which is taken from Galbany et al. (2019) Table 3.

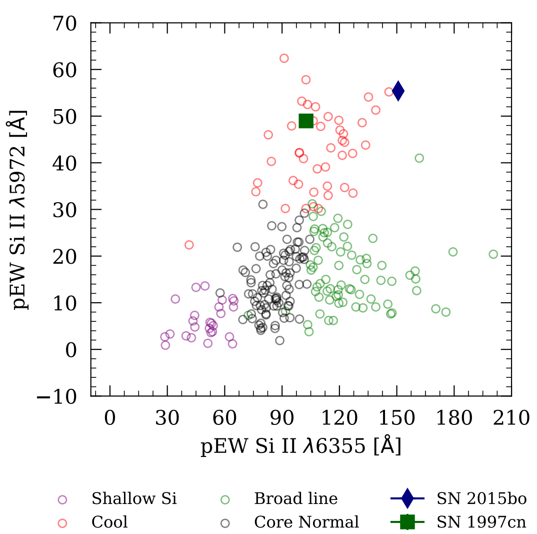

Figure 14. Branch diagram (Branch et al. 2006) with SN 2015bo as the blue diamond and SN 1997cn as the dark green square.

Expansion velocities for each strong spectral feature present in the spectra of SN 2015bo are shown in Figure 15 along with velocities from other SNe Ia for comparison. There are four sub-luminous SNe (SN 1991bg, SN 1999by, SN 2005bl, SN 2005ke) and two normal SNe (SN 2011fe and SN 2014J). Comparison velocities are taken from Galbany et al. (2019), and shaded regions represent the Cool and Broad Line regions from Folatelli et al. (2013). Uncertainties are derived from both the uncertainty in the measurement of the minimum of the feature and the resolution limit of the respective instrument used to observe each spectrum. These two uncertainties are added in quadrature to derive the final uncertainty.

For the Ca II H&K feature, SN 2015bo starts at $\sim$18,000 km s^{-1} $\sim$+8 d before B-band maximum near the normal SNe and decreases over time to reach $\sim$13,000 km s^{-1} at $\sim$+31 d after maximum to be among the sub-luminous SNe. This evolution does not mirror other sub-luminous SNe Ia in the sample, which have a flatter velocity evolution going from $\sim$13,000 km s^{-1} at early times to $\sim$11,000 km s^{-1} at later times. The evolution occupies the same space as the Cool region after ~ -5 d.

At early times, S II W-blue feature's velocity is similar to SN 2005bl and SN 2014J. The velocity evolution follows the Cool and other 1991bg-like SNe. The evolution has an initial velocity of $\sim$11,000 km s^{-1} similar to SN 2005bl, however, this drops to $\sim$6,000 km s^{-1} which is similar to other sub-luminous SNe Ia. The S II W-red feature shows analogous behavior; it starts near SN 2005bl and SN 2014J and declines over time to match the other sub-luminous Ia.

SN 2015bo has the fastest Si II λ 5972 feature of the sample at $\sim$13,500 km s^{-1}. This is in the Broad Line region. It then slows down until it is slower than all the other SNe. Unlike the S II W-red feature, which reaches a homogenous value at ~ -5 d, the Si II λ 5972 feature continues to decline until it is the lowest velocity SN in the sample.

At ~ -8 d, SN 2015bo starts faster than all other sub-luminous SNe Ia Si II λ 6355 velocities with the exception of SN 2005bl at $\sim$15,000 km s^{-1}. After declining, the velocities are consistent with other fast-declining SNe Ia and are in the Cool region. At $\sim$+31 d, it is slower than any other member of the comparison sample with a velocity of $\sim$5,000km s^{-1}.

The two features of Si II λ 5972 and Si II λ 6355 exhibit velocities that diverge downwards from the Cool pathway of Folatelli et al. (2013) between $\sim$0 d to $\sim$+5 d and $\sim$+10 d to $\sim$+20 d past maximum, respectively. These lower velocities also suggest that the base of the Silicon is deeper in SN 2015bo in all other SNe Ia in the sample.

While noticeable residuals in the corrections for the telluric features are not seen in the epochs with calculated O I λ 7774 velocities, they still might exert influ-

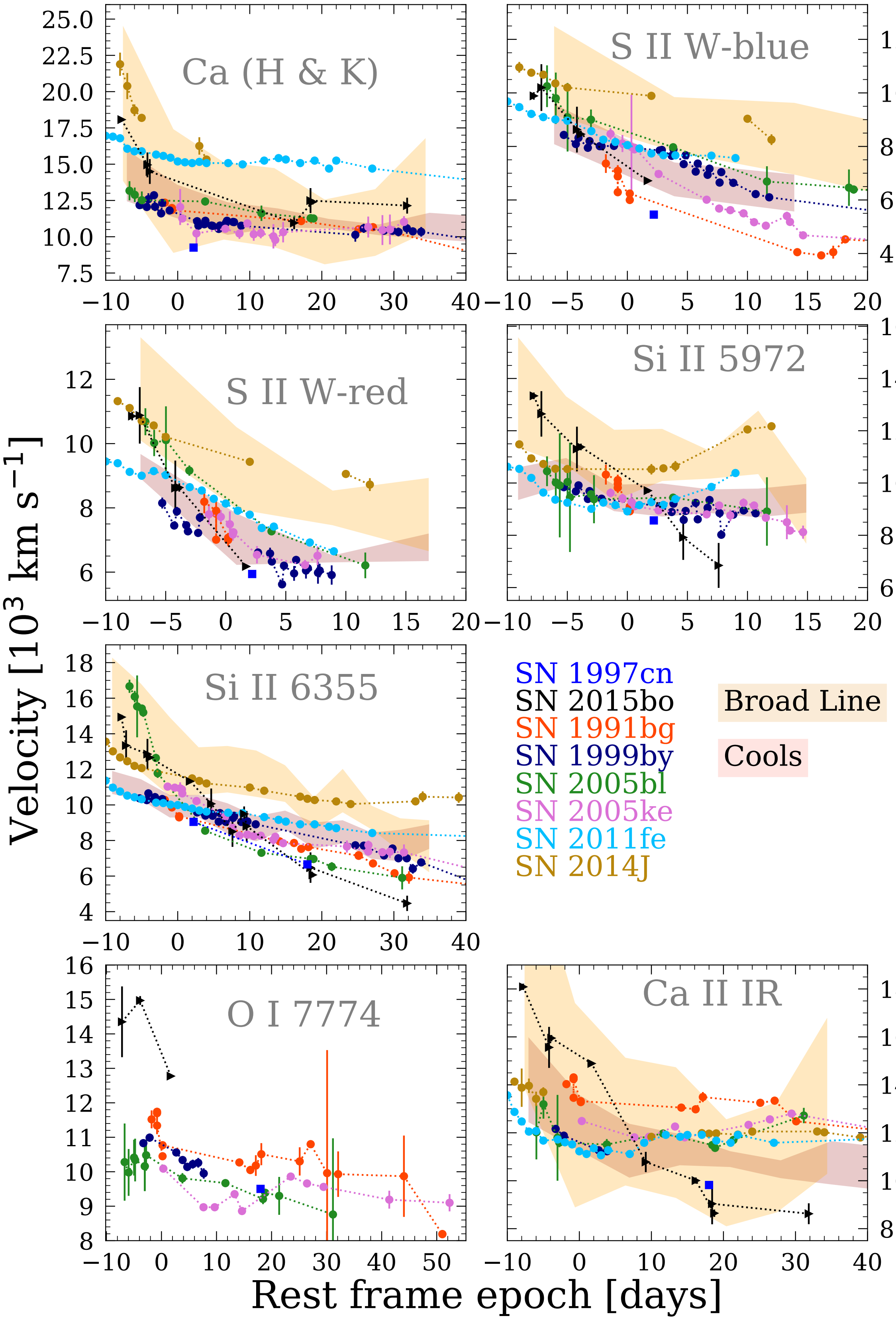

Figure 15. Velocities of SN 1997cn (blue squares), SN 2015bo (black, left-facing triangles) and other SNe Ia (other colors, circles). The tan and salmon shaded areas are the 1σ dispersion regions of the Broad Line and Cool evolutionary paths presented in Folatelli et al. (2013) using CSP-I data.

ence on the calculations. This potential influence can be seen in significant difference between SN 2015bo and the rest of the comparison sample. However, if these mesaurements are correct and do not suffer from telluric absoption, then SN 2015bo has the fastest velocities of the sample.

Finally, SN 2015bo's Ca II IR velocity is 18,000 km s^{-1} at ~ -10 d, the highest velocity in the entire sample. However, it declines rapidly from $\sim$0 d to $\sim$+10 d – SN 2015bo transitions from being the fastest to the slowest in that time period. After $\sim$+10 d, SN 2015bo declines only slightly over the next twenty days to $\sim$8,500 km s^{-1} at +31 d after max.

Overall, the velocities are unique in their steep declines. SN 2015bo starts on the higher end of the 1991bg-like SNe and then finishes on the lower end of the 1991bg-like SNe distribution in nearly every panel of Figure 15. Additionally, SN 2015bo primarily resides outside the Cool region. This behavior is unique to SN 2015bo. Along with the different $V - r$ color curve, this behavior gives evidence that SN 2015bo is different than other 1991bg-like objects.

4.3.3. *Pseudo-Equivalent Widths*

The pEWs for SN 2015bo and selected comparison SNe Ia are plotted in Figure 16. The pEW in Ca II H&K for SN 2015bo is homogenous with the comparison sample even though SN 2015bo starts larger than any other Cool SN with a value of $\sim$130 Å. The wavelength coverage of the spectra from $\sim$0 d to $\sim$+16 d did not fully capture the feature, so it is uncertain what value SN 2015bo would decline to, if at all. At $\sim$+31 d after maximum, SN 2015bo has the largest value at $\sim$115 Å.

In Fe II, SN 2015bo is uniform with the rest of the sample, however, SN 2015bo exhibits a higher maximum value of $\sim$425 Å at $\sim$+15 d.

The S II W pEW deviates from the rest of the sample; it starts near SN 2011fe at $\sim$75 Å but drops below SN 2014J to $\sim$60 Å at ~ -5 d. This is followed by a slight increase to $\sim$70 Å five days prior to B-band maximum. At $\sim$+2 d after maximum, SN 2015bo declines down to $\sim$60 Å. This evolution is not seen in any of the comparison SNe – normal or sub-luminous. SN 2015bo inhabits the Cool region.

In Si II λ 5972, sub-luminous SNe have a concave down morphology and normal SNe have a concave up morphology. This is an effect of temperature and the heating of the photopshere. Since SN 2015bo is sub-luminous, it has a concave down form; it starts at $\sim$45 Å, which is greater than the rest of the comparison collection, and then increases to a peak of $\sim$55 Å at $\sim$+3 d after maximum. From there, SN 2015bo declines slightly to $\sim$35 Å. The decline for SN 2015bo at $\sim$+5 d after maximum is earlier than the other sub-luminous SNe, but this time, perhaps coincidentally, corresponds to the rise of SN 2011fe. SN 2015bo occupies a similar area as the Broad Line region.

SN 2015bo has the same evolution curve as the rest of the sample in Si II λ 6355, however, its numerical values are marginally higher. SN 2015bo's maximum m$_B$ time at $\sim$+20 d after maximum is consistent with the peak of SN 1991bg and SN 2005bl, however, both SN 1999by and SN 2005ke peak later by $\sim$10 d. The largest pEW value of $\sim$235 Å is larger than the four SNe Ia just mentioned – they peak at $\sim$180-195 Å. The only SN in the comparison sample that has a higher pEW is SN 2014J with a value of $\sim$255 Å. This value occurs later than SN 2015bo's at $\sim$+35 d. Beyond $\sim$+25 d, we expect that the line is blended with Fe II and not just solely Si II emission.

In O I λ 7774, SN 2015bo starts well above the rest of the sample SNe Ia at almost 220 Å ~ -8 d, but it returns to a more consistent value of $\sim$130 Å at t$(B)_{\rm max}$. The pEW in O I may suffer from telluric absorption even though only epochs without obvious telluric contamination were selected.

Finally, SN 2015bo starts marginally higher at $\sim$310 Å at ~ -8 d in Ca II IR, but quickly integrates itself into the mean path of the sample $\sim$+10 d after maximum at $\sim$310 Å and rises to reach $\sim$460 Å at $\sim$+31 d after maximum.

4.4. *Near Infrared Spectrum*

The presented NIR spectrum was observed at +11.5 d and is shown in Figure 17. We identify Ca II $\lambda\lambda$ 8662, 8538, Mg II $\lambda\lambda$ 9227, 10927, Si II λ 11737, Ca II $\lambda\lambda$ 11839, 11950, and Fe II features, as well as significant Fe and Co emission between the two telluric bands in the H-band break. Finally, strong Co II emission is present in the 2 μm to 2.4 μm region. Eight Co II lines dominate this region: Co II $\lambda\lambda$ 20913, 21211, 21351, 21509, 22209, 22482, 23619, 24603 (Gall et al. 2012).

There is an area of strong Fe II, Co II, and Ni II emission known as the H-band break that originates from allowed transitions above the photosphere (Wheeler et al. 1998). Hsiao et al. (2013) found a correlation between the SN stretch parameter and the feature strength of the H-band break and that the H-band break strength should be near its maximum value at the phase of our observed NIR spectrum. Ashall et al. (2019a,b) showed that this feature can be used to determine the location of the outermost ^{56}Ni in SNe Ia using the v_{edge} parameter. The v_{edge} parameter is the velocity of the bluest edge of the H-band break Co II emission line – see Ashall et al.

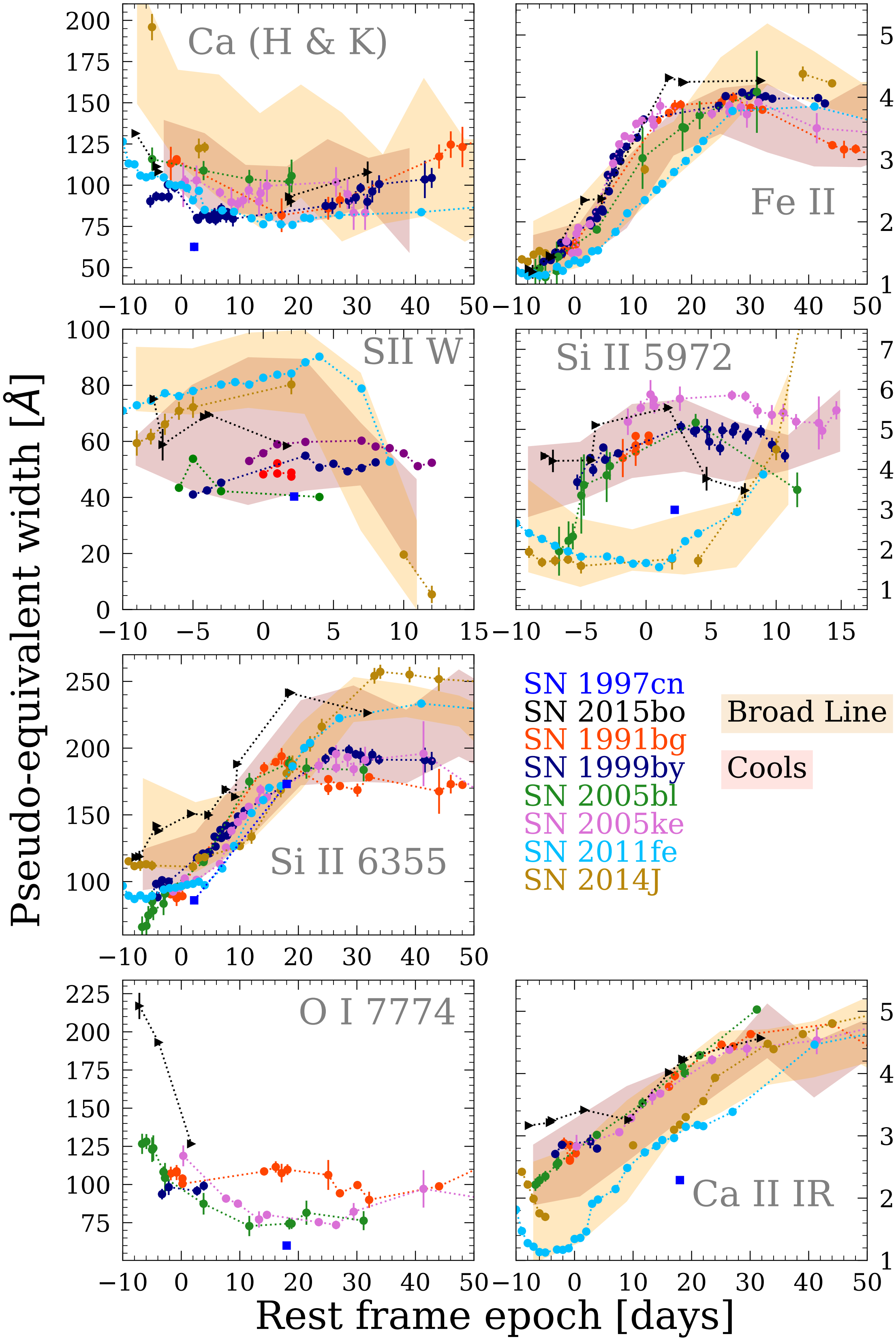

Figure 16. Pseudo-equivalent widths of SN 1997cn (blue, squares) SN 2015bo (black, left-facing triangles) and other SNe Ia (other colors, circles). The tan and salmon shaded areas are the 1σ dispersion regions of the Broad Line and Cool evolutionary paths presented in Folatelli et al. (2013) using CSP-I data.

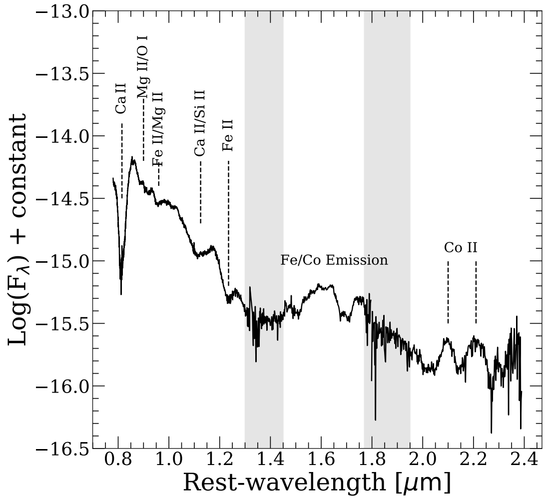

Figure 17. NIR spectrum of SN 2015bo at +11.5 d. Telluric regions are denoted by grey bands. Spectral features are labeled on the plot and described in the text.

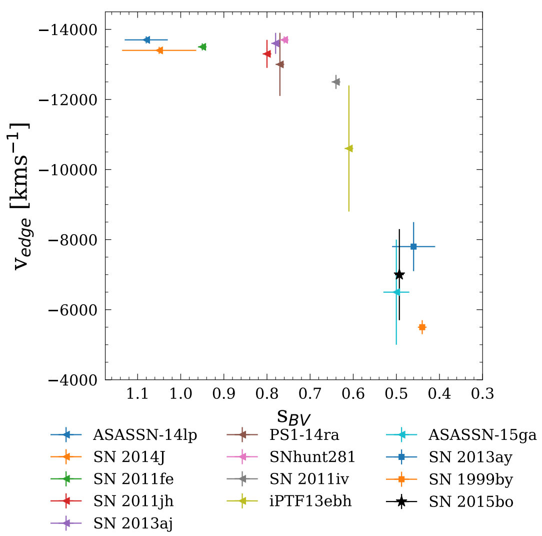

Figure 18. v_{edge} versus s_{BV} plot using data from Ashall et al. (2019b). v_{edge} is the velocity of the bluest Co II emission line in the H-band break.

(2019a) for further details. v_{edge} is plotted against s_{BV} in Figure 18 using data from Ashall et al. (2019a).

SN 2015bo's v_{edge} is 7000 ± 1300 km s^{-1} (Ashall et al. 2019b). This shows that the majority of the ^{56}Ni mass is located in the center of the ejecta. This also implies a low ^{56}Ni mass as found in §3.4.

5. DISTANCE TO NGC 5490 & 1991BG-LIKE SNE AS DISTANCE INDICATORS

SN 2015bo has a sibling (a SN in the same host galaxy) – SN 1997cn (Li et al. 1997; Turatto et al. 1998b; Jha et al. 2006). Interestingly, SN 2015bo and SN 1997cn are also both fast decliners, so not only are they siblings, they are also spectrally similar (nominally called "twins"). Since fast decliners are located preferentially in early-type galaxies (Hamuy et al. 1996), it is unsurprising that both SNe in NGC 5490 are fast decliners. This provides an opportunity to evaluate the accuracy and consistency of these quasi-rare sub-types as distance indicators. To date, this is the only known instance of two fast-declining SNe exploding in the same host galaxy. In this section, distance modulii are derived using various methods and checked for consistency.

Table 4. Distance modulii derived using four independent methods: z_{cmb} cosmology, surface-brightness fluctuations, SN 2015bo, and SN 1997cn.

Object	μ [mag]	σ_μ [mag]
NGC 5490[a]	34.30	0.15
NGC 5490[b]	34.27	0.08
SN 2015bo	34.33	0.01 (stat) 0.13 (sys)
SN 1997cn	34.34	0.04 (stat) 0.12 (sys)

[a]Corrected to the CMB rest frame and calculated using H_0=73 km s^{-1} Mpc^{-1}, Ω_m=0.27 and Ω_Λ=0.73, which is used throughout this work.

[b]Distance derived from surface brightness fluctuation distance from Jensen et al. (2021)

We calculate the distance modulus to the host (NGC 5490) with three independent methods: i) the z_{cmb} distance derived method assuming a cosmology of H_0=73 km s^{-1} Mpc^{-1}, Ω_m=0.27 and Ω_Λ=0.73, ii) the independent distance derived using the photometry of all available bands of SN 2015bo, and iii) the independent distance derived using the photometry of all available bands of SN 1997cn. All of the derived distances, as well as the distance computed using surface-brightness fluctuations (Jensen et al. 2021), can be found in Table 4.

The distance modulus derived using the z_{cmb} method is $\mu = 34.30 \pm$ 0.15 mag. As discussed in §3.1, the distance modulus to SN 2015bo was determined using the EBV2 model and a 1991bg-like K-correction in SNooPy. Photometry for SN 2015bo is in the CSP natural system. The distance modulus from this calculation is $\mu = 34.36 \pm 0.01$ (stat) $\pm$ 0.13 (sys) mag. The initial fit in SNooPy also gives a significant host galaxy extinction of $E(B-V) = 0.21 \pm 0.01 \pm 0.06$. However, SN 2015bo is in an E-type galaxy, more than an arcminute away from the center of the galaxy, and does not show a narrow Na I feature in any of the spectra. Therefore, the systematic uncertainty due to the uncertainty in the amount of extinction must be calculated.

SNooPy has an uncertainty budget described in Burns et al. (2011). Of the four categories, only the uncertainty from reddening and the stretch parameter apply here. The systematic uncertainty from reddening was determined via two methods. The first method took the systematic uncertainty as the difference between distance modulus when calculated with $E(B-V)$ as a free parameter and held fixed to a value of 0. This gave a systematic uncertainty in distance modulus of ± 0.01 mag for SN 1997cn and ± 0.06 mag for SN 2015bo. The second method was to use the intrinsic dispersion in the B-V intrinsic color. The dispersion is ± 0.06, so one could also simply adopt that as a systematic. This gives uncertainties of ± 0.04 mag and ± 0.06 mag in distance modulus for SN 1997cn and SN 2015bo, respectively. The method with the larger value was chosen to be used in the final analysis.

To compute the systematic uncertainty for s_{BV}, the dispersion in the fit between s_{BV} and $\Delta m_{15}(B)$ is considered. Because these are independent measures of the decline rate, the source of the dispersion in this relation comes from both random noise (due to measurement error) and any systematic errors that s_{BV} and $\Delta m_{15}(B)$ have in measuring the "true" decline rate. Therefore the dispersion is an upper limit on the systematic error in s_{BV} (or $\Delta m_{15}(B)$). This value is $\sigma s_{BV} = 0.03$, which turns into an uncertainty in distance modulus of ± 0.11 mag. These values from the reddening and the color-stretch parameter are then added in quadrature for both objects to arrive at their respective total systematic uncertainties.

The standard system filters are used when fitting the photometry of SN 1997cn with SNooPy because the data for SN 1997cn is in the standard system. Additionally, since there is not enough photometric data to accurately determine $t(B)_{\rm max}$, the best spectrum for SN 1997cn was used as input in SNID to determine the time of maximum using the spectrum. The best SNID match was to SN 1998de at +2.7 d old. The time from this match ($t(B)_{\rm max}$= 50587.8 MJD) was then given to SNooPy to use as the time of B-band maximum. Without constraining $t(B)_{\rm max}$, SNooPy struggles to fit the light curves. This is because SNooPy seeks to fit the I-band with two maxima like normal SNe Ia, however, SN 1997cn does not have a second maximum. This causes the fit to be poor. Apart from these differences, the fitting methods used to derive the distance modulus of SN 1997cn are the same as the ones used

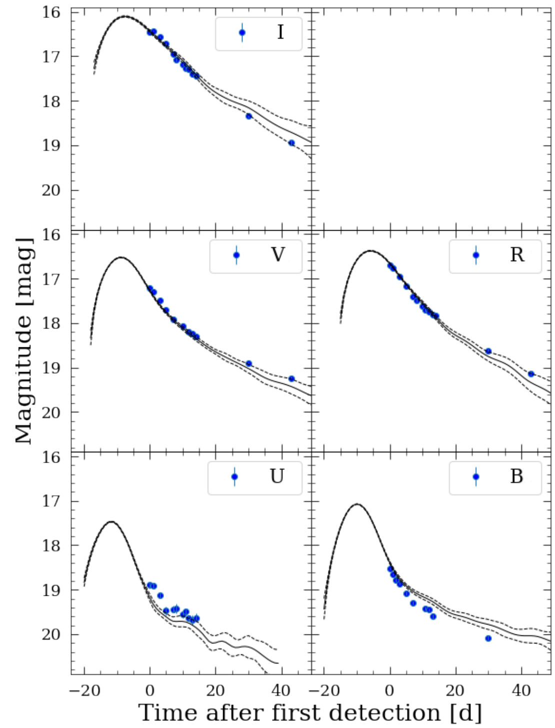

Figure 19. SNooPy fits for SN 1997cn. Data from Jha et al. (2006). The fits are constrained by using the $t(B)_{\rm max}$ from SNID.

to derive the distance modulus of SN 2015bo. Only the data from Jha et al. (2006) was used because it was obtained on a single telescope and published in the standard system. Turatto et al. (1998b) use data from multiple telescopes and it is unclear what system the data is in. Fits for SN 1997cn are presented in Figure 19. The distance modulus derived from SNooPy is $\mu = 34.37 \pm 0.04$ (stat) ± 0.12 (sys) mag.

Adding the statistical and systematic errors in quadrature for SN 1997cn and SN 2015bo gives values of $\mu_{97cn} = 34.37 \pm 0.13$ mag and $\mu_{15bo} = 34.36 \pm 0.13$ mag. The difference in distance modulus is $\Delta\mu = 0.01 \pm 0.19$ mag, again with the errors added in quadrature. The distances differ by less than 0.06-σ.

Figure 20 provides a visual representation of the distance modulii where the consistency is clearly seen. Additionally, distance modulii from both redshift-corrected cosmology and surface-brightness fluctuations from Jensen et al. (2021). Note that there is most likely further uncertainty due to fits for SN 1997cn being poorly constrained from the lack of data prior to maximum in all bands. This will add in an extra uncertainty in the value for SN 1997cn. Therefore, the presented values are lower bounds for the uncertainty. Considering this, it appears that fast decliners might be equally standardizable as normal SNe Ia and could offer the same

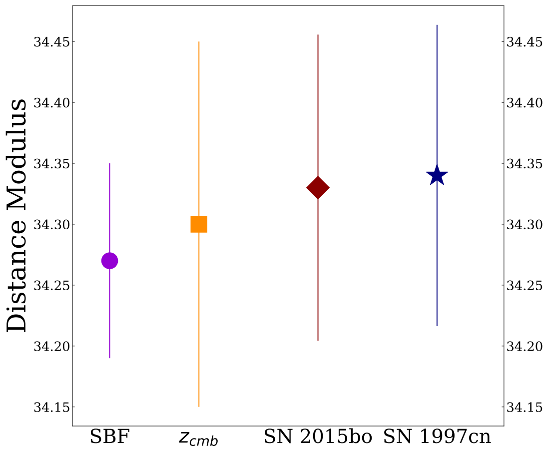

Figure 20. Graphical comparison of distance modulii derived from surface brightness fluctuation (SBF; taken from Jensen et al. 2021), z_{cmb}-corrected cosmology, SN 2015bo, and SN 1997cn. All values are consistent with each other.

robust functionality. The result from Burns et al. (2018) supports this hypothesis – they found SN 2006mr to be consistent with three other SNe Ia in Fornax A.

However, there have been inconsistencies in the past with using twins and siblings when deriving distances. Foley et al. (2020) found a significant ($\delta \mathrm{M}_V = 0.335 \pm 0.069$ mag) difference between the peak V-band magnitudes of 2011by and 2011fe, but these SNe were hosted by different galaxies – NGC 3972 and M101, respectively – they may be influenced by peculiar velocities. Gall et al. (2018) found that two transitional supernovae (SN 2007on and SN 2011iv) that exploded in the same host galaxy produce a statistical difference in calculated distance modulii in both B- and H-bands. They found the two objects' distance moduli differed by $\sim$14% and $\sim$9% in the B- and H-bands, respectively. On the other hand, SN 2015bo and SN 1997cn are in the same host galaxy, have similar spectra, and have consistent distances. This tension can be resolved with further twin studies of fast decliners.

The maximum light spectral similarity of SN 1997cn and SN 2015bo can be seen in Figure 21. The 'twinness' parameter described by Fakhouri et al. (2015) was calculated to be 1.04, which puts it in the median range of twinness. This parameter is akin to a reduced χ^2 parameter, and therefore it is sensitive to estimated errors. This estimated error dominates the spectra possibly due to the data being taken on different telescopes and instruments, and thus the twinness parameter may not be the best indicator of how alike two spectra or SNe Ia are unless the quality of the input data is similar.

6. CONCLUSION

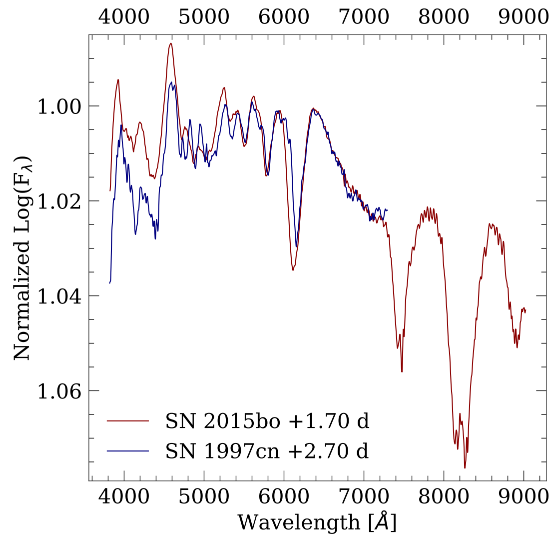

Figure 21. Comparison of the spectra of SN 1997cn (navy) and SN 2015bo (dark red). The spectra have been color corrected to match the photometric observations, put through a Gaussian 3-σ smoothing function, and were normalized to the blue edge of the Si II λ 6355 feature.

Photometric $uBVgriYHJ$ data of SN 2015bo from -2.9 d to $+103.8$ d and spectroscopic data from -7.8 d to 31.8 d from maximum light are presented. SN 2015bo is a fast-declining, under-luminous SN Ia that exploded in NGC 5490. SN 2015bo has an absolute magnitude $M_B = -17.50 \pm 0.13$ mag. It has $\Delta \mathrm{m}_{15}$(B)= 1.91$\pm$0.01 (mag) and s_{BV}= 0.48 $\pm$ 0.01.

Photometrically, SN 2015bo is sub-luminous and fast-declining, and it occupies the same parameter space as other under-luminous, fast decliners in the luminosity-width relation. This is confirmed in the s_{BV} versus t^{i-B}_{max} diagram where SN 2015bo is positioned among 1991bg-like SNe. The light-curves evolve quickly, and SN 2015bo has unique morphologies in the $V - r$ and $r - i$ color-curves. In the $V - r$ color-curve, it is the bluest SNe in the plotted sample even with extinction corrections applied. In the $r - i$ color-curve, it displays a redward climb at $\sim$+40 d. This may be a way to identify peculiar sub-luminous SNe in future surveys. SN 2015bo has a peak bolometric luminosity of $L^{peak}_{bolo} = 0.34 \pm 0.03 \times 10^{43}$ erg s^{-1}, which corresponds to a nickel mass of $0.17 \pm 0.03 M_\odot$. This value may change slightly if the full Arnett's rule and a rise time were used.

Spectroscopically, SN 2015bo shows the standard features typical for a fast decliner. In the Branch et al. (2006) diagram, SN 2015bo resides among other Cool SNe Ia. SN 2015bo's velocities range from $\sim$18,000km s^{-1}to $\sim$4,000km s^{-1} and decrease over time.

Importantly, SN 2015bo exploded in the same host galaxy as SN 1997cn, another fast decliner. Distances to both SN 2015bo and SN 1997cn were calculated and are consistent with each other to the 0.25σ level. We suggest that fast decliners are consistent and standardizable, and hence they should *not* be omitted from future cosmological work. A future study of two or more fast-declining siblings with two or more well sampled objects will offer a chance to confirm this result.

APPENDIX

A. SN 1997cn LIGHT CURVES

Light curves for SN 1997cn are presented in Figure A1, as well as $t(B)_{max}$ as derived from SNooPy, SNID spectrum analysis, and the spectral modelling performed by Turatto et al. (1998a). Turatto et al. (1998b) estimate B-band maximum occurred on 1997 May 19 (2450587.50 JD) which is +18 d after the inferred explosion. The time derived by SNooPy using data from Jha et al. (2006) is 2450580.72 ± 0.70 JD. The difference is $\Delta t(B)_{max}$= 6.78 d. The SNooPy $t(B)_{max}$ is before the discovery point, however, the discovery point could be close to maximum. Given that the data was taken without a filter, it most likely resembles V- or R-band photometry. The SNID $t(B)_{max}$ is 2450588.3 JD. This time yields the best SNooPy fits of the light curves. SNooPy differs from these dates because there is no well-defined maximum in the light curves for SN 1997cn. The exact date of maximum is uncertain. This comes from the fact that comprehensive, all-sky surveys for SNe were not available when SN 1997cn exploded.

B. PHOTOMETRIC DATA

Table B1. Log of optical photometric data.

day [MJD]	u [mag]	B [mag]	V [mag]	g [mag]	r [mag]	i [mag]
57069.4	18.51(0.03)	17.49(0.01)	17.30(0.01)	17.35(0.01)	17.21(0.01)	17.49(0.01)
57075.4	18.16(0.02)	16.84(0.01)	16.52(0.01)	16.63(0.01)	16.37(0.01)	16.66(0.01)
57076.3	18.24(0.02)	16.86(0.01)	16.47(0.01)	16.63(0.01)	16.32(0.01)	16.65(0.01)
57079.4	18.55(0.03)	17.08(0.01)	16.48(0.01)	16.76(0.01)	16.28(0.01)	16.64(0.01)
57080.3	18.66(0.03)	17.22(0.01)	16.51(0.01)	16.86(0.01)	16.30(0.01)	16.65(0.01)
57082.3	···	17.55(0.01)	16.66(0.01)	17.13(0.01)	···	···
57082.4	19.07(0.03)	···	···	···	16.37(0.01)	16.72(0.01)
57083.3	19.22(0.04)	17.71(0.01)	16.74(0.01)	17.28(0.01)	16.44(0.01)	16.75(0.01)
57084.3	19.41(0.05)	17.90(0.02)	16.84(0.01)	17.46(0.02)	16.50(0.01)	16.79(0.02)
57085.3	19.62(0.06)	18.05(0.02)	16.96(0.02)	17.59(0.02)	16.56(0.01)	16.78(0.01)
57086.3	···	···	17.10(0.02)	17.76(0.02)	16.65(0.01)	16.83(0.01)
57086.4	···	18.15(0.02)	···	···	···	···
57087.3	···	18.32(0.03)	17.16(0.01)	17.93(0.02)	16.71(0.01)	16.83(0.01)
57087.4	19.76(0.15)	···	···	···	···	···
57088.3	···	18.45(0.02)	17.27(0.02)	18.02(0.02)	16.77(0.01)	16.86(0.02)
57089.3	···	18.59(0.03)	17.37(0.02)	18.18(0.02)	16.85(0.01)	16.88(0.01)
57090.4	···	18.70(0.03)	17.45(0.02)	18.27(0.02)	16.92(0.01)	16.93(0.01)
57091.3	···	18.79(0.02)	17.56(0.01)	18.36(0.02)	16.99(0.01)	16.97(0.01)
57092.4	···	18.83(0.03)	17.65(0.02)	18.42(0.02)	17.06(0.01)	17.04(0.01)
57093.3	···	19.00(0.02)	17.70(0.01)	18.54(0.02)	17.16(0.01)	17.10(0.01)

Table B1 *continued*

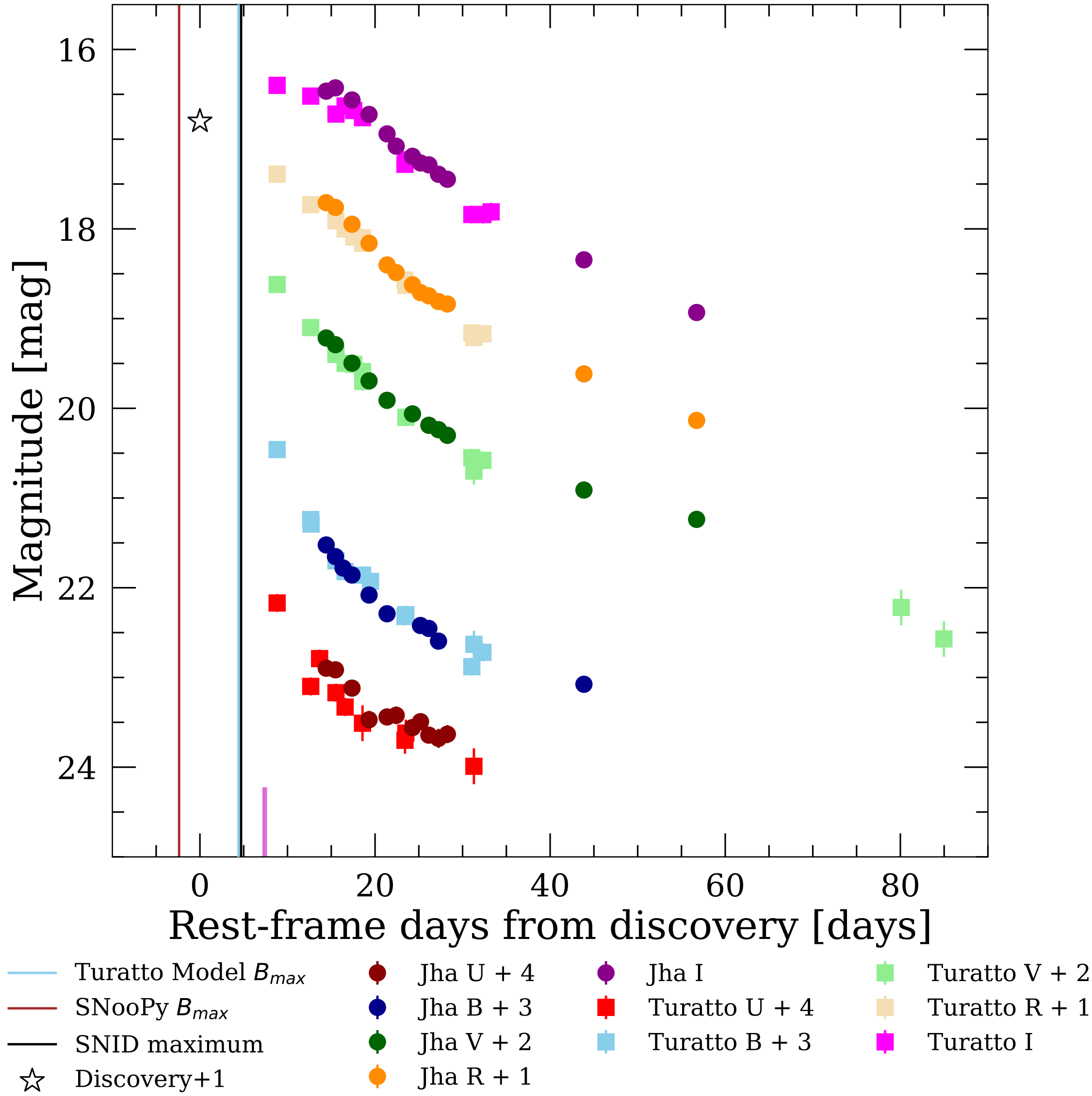

Figure A1. Light curves of SN 1997cn using data from Li et al. (1997) (discovery), Turatto et al. (1998b) (lightly colored points), and Jha et al. (2006) (darker colored points). The discovery point from Li et al. (1997) uses an unfiltered CCD exposure. This point is plotted as if it was in the R-band. The magenta line represents the date of the earliest spectrum for SN 1997cn.

Table B1 *(continued)*

day [MJD]	u [mag]	B [mag]	V [mag]	g [mag]	r [mag]	i [mag]
57094.3	...	19.01(0.02)	17.82(0.02)	...	...	...
57094.4	...	...	...	18.62(0.02)	17.23(0.01)	17.17(0.01)
57095.3	...	19.08(0.02)	17.88(0.01)	18.68(0.02)	...	...
57095.4	...	...	...	...	17.32(0.01)	17.24(0.01)
57096.3	...	19.14(0.02)	17.97(0.02)	...	...	...
57096.4	...	...	...	18.75(0.02)	17.42(0.01)	17.32(0.01)

Table B1 *continued*

Table B1 *(continued)*

day [MJD]	u [mag]	B [mag]	V [mag]	g [mag]	r [mag]	i [mag]
57097.3	···	···	···	18.83(0.02)	17.52(0.01)	···
57097.4	···	19.24(0.02)	18.04(0.02)	···	···	17.44(0.01)
57098.3	···	···	···	18.88(0.02)	17.62(0.01)	17.54(0.01)
57098.4	···	19.25(0.02)	18.14(0.02)	···	···	···
57099.3	···	19.32(0.02)	18.20(0.02)	18.89(0.02)	17.70(0.01)	17.62(0.01)
57100.3	···	19.39(0.02)	18.27(0.02)	19.00(0.02)	17.79(0.01)	17.71(0.01)
57101.3	···	19.46(0.02)	18.33(0.01)	19.04(0.02)	17.84(0.01)	17.79(0.01)
57102.3	···	19.49(0.02)	18.38(0.02)	19.11(0.02)	17.89(0.01)	17.84(0.02)
57103.4	···	···	18.42(0.04)	19.13(0.04)	17.81(0.06)	···
57104.3	···	···	···	···	18.00(0.02)	···
57109.3	···	···	···	···	18.23(0.01)	···
57109.4	···	19.67(0.02)	18.62(0.02)	19.27(0.02)	···	18.24(0.02)
57110.2	···	···	···	19.34(0.02)	18.29(0.01)	···
57110.3	···	19.69(0.02)	18.68(0.02)	···	···	18.30(0.02)
57111.3	···	19.76(0.02)	18.71(0.02)	19.36(0.02)	18.33(0.01)	18.39(0.02)
57112.3	···	19.66(0.02)	18.73(0.02)	19.37(0.02)	18.38(0.01)	18.39(0.01)
57113.3	···	19.74(0.05)	18.77(0.02)	19.37(0.04)	18.42(0.02)	18.47(0.02)
57117.2	···	···	···	19.40(0.06)	18.58(0.03)	···
57117.3	···	19.76(0.09)	18.91(0.05)	19.45(0.06)	···	18.64(0.03)
57119.3	···	19.76(0.07)	18.96(0.04)	···	18.64(0.02)	18.73(0.03)
57121.2	···	19.92(0.04)	19.00(0.02)	19.54(0.03)	18.72(0.02)	18.79(0.02)
57123.3	···	20.00(0.04)	19.05(0.02)	19.55(0.02)	18.82(0.02)	18.88(0.02)
57126.2	···	20.03(0.02)	19.17(0.02)	···	···	···
57126.3	···	···	···	19.64(0.02)	18.98(0.02)	19.04(0.02)
57129.2	···	20.05(0.02)	19.26(0.02)	19.67(0.02)	19.08(0.02)	19.16(0.02)
57131.3	···	20.07(0.02)	19.32(0.02)	19.70(0.02)	19.15(0.02)	19.21(0.02)
57134.3	···	20.10(0.03)	19.38(0.02)	19.77(0.02)	19.30(0.02)	19.30(0.03)
57136.3	···	20.13(0.03)	19.42(0.02)	19.81(0.02)	19.35(0.02)	19.40(0.03)
57138.2	···	20.16(0.03)	19.50(0.02)	19.84(0.02)	19.42(0.02)	19.45(0.02)
57153.2	···	20.43(0.04)	19.85(0.03)	20.10(0.03)	20.05(0.03)	19.94(0.05)
57160.2	···	20.61(0.04)	20.04(0.03)	20.18(0.03)	20.26(0.04)	20.15(0.07)
57180.1	···	···	···	20.61(0.04)	20.98(0.07)	···
57181.2	···	···	···	20.50(0.09)	···	···
57182.1	···	···	20.38(0.09)	20.60(0.07)	···	···

Table B2. Log of near-infrared photometric data.

day [MJD]	J [mag]	H [mag]	Y [mag]
57088.3	16.97(0.02)	16.51(0.02)	16.30(0.01)
57089.4	16.97(0.03)	16.53(0.02)	16.31(0.01)
57090.4	17.00(0.03)	16.59(0.02)	16.31(0.01)
57091.3	17.06(0.03)	16.57(0.02)	16.32(0.01)
57093.3	17.15(0.02)	16.72(0.02)	16.35(0.01)

ACKNOWLEDGMENTS

WBH acknowledges support from Research Experience for Undergraduates program at the Institute for Astronomy, University of Hawaii-Manoa funded through NSF grant #2050710. L.G. acknowledges financial support from the Spanish Ministry of Science, Innovation and Universities (MICIU) under the 2019 Ramón y Cajal program RYC2019-027683 and from the Spanish MICIU project PID2020-115253GA-I00. M. G. M., R. G. D., and S. M. T. were funded by the European Union's Horizon 2020 research and innovation programme under the Marie Skłodowska-Curie grant agreement No. 839090. Based on observations collected at the European Southern Observatory under ESO programme 106.2104. The work of the CSP-II has been generously supported by the National Science Foundation under grants AST-1008343, AST-1613426, AST-1613455, and AST-1613472. The CSP-II was also supported in part by the Danish Agency for Science and Technology and Innovation through a Sapere Aude Level 2 grant. E.B. was partially supported by NASA Grant 80NSSC20K0538

J.D.L acknowledges support from a UK Research and Innovation Fellowship (MR/T020784/1). C.R.B. acknowledges support from NSF grants AST-1008384, AST-1613426, AST-1613455, and AST-1613472.

REFERENCES

Adelman-McCarthy, J. K., Agüeros, M. A., Allam, S. S., et al. 2008, ApJS, 175, 297, doi: 10.1086/524984

Arnett, W. D. 1982, ApJ, 253, 785, doi: 10.1086/159681

Ashall, C., Mazzali, P. A., Pian, E., & James, P. A. 2016, MNRAS, 463, 1891, doi: 10.1093/mnras/stw2114

Ashall, C., Mazzali, P. A., Stritzinger, M. D., et al. 2018, MNRAS, 477, 153, doi: 10.1093/mnras/sty632

Ashall, C., Hsiao, E. Y., Hoeflich, P., et al. 2019a, ApJL, 875, L14, doi: 10.3847/2041-8213/ab1654

Ashall, C., Hoeflich, P., Hsiao, E. Y., et al. 2019b, ApJ, 878, 86, doi: 10.3847/1538-4357/ab204b

Ashall, C., Lu, J., Burns, C., et al. 2020, ApJL, 895, L3, doi: 10.3847/2041-8213/ab8e37

Ashall, C., Lu, J., Hsiao, E. Y., et al. 2021, arXiv e-prints, arXiv:2106.12140. https://arxiv.org/abs/2106.12140

Bacon, R., Accardo, M., Adjali, L., et al. 2010, in Society of Photo-Optical Instrumentation Engineers (SPIE) Conference Series, Vol. 7735, Ground-based and Airborne Instrumentation for Astronomy III, ed. I. S. McLean, S. K. Ramsay, & H. Takami, 773508, doi: 10.1117/12.856027

Benetti, S., Meikle, P., Stehle, M., et al. 2004, MNRAS, 348, 261, doi: 10.1111/j.1365-2966.2004.07357.x

Benetti, S., Cappellaro, E., Mazzali, P. A., et al. 2005, ApJ, 623, 1011, doi: 10.1086/428608

Betoule, M., Kessler, R., Guy, J., et al. 2014, A&A, 568, A22, doi: 10.1051/0004-6361/201423413

Blondin, S., Dessart, L., & Hillier, D. J. 2015, MNRAS, 448, 2766, doi: 10.1093/mnras/stv188

—. 2018, MNRAS, 474, 3931, doi: 10.1093/mnras/stx3058

Branch, D., Dang, L. C., Hall, N., et al. 2006, PASP, 118, 560, doi: 10.1086/502778

Brown, P. 2014, in Proceedings of Swift: 10 Years of Discovery (SWIFT 10, 125. https://arxiv.org/abs/1505.01368

Burns, C. R., Stritzinger, M., Phillips, M. M., et al. 2011, AJ, 141, 19, doi: 10.1088/0004-6256/141/1/19

—. 2014, ApJ, 789, 32, doi: 10.1088/0004-637X/789/1/32

Burns, C. R., Parent, E., Phillips, M. M., et al. 2018, ApJ, 869, 56, doi: 10.3847/1538-4357/aae51c

Burns, C. R., Ashall, C., Contreras, C., et al. 2020, ApJ, 895, 118, doi: 10.3847/1538-4357/ab8e3e

de Vaucouleurs, G., de Vaucouleurs, A., Corwin, Herold G., J., et al. 1991, Third Reference Catalogue of Bright Galaxies

Diamond, T. R., Hoeflich, P., Hsiao, E. Y., et al. 2018, ApJ, 861, 119, doi: 10.3847/1538-4357/aac434

Dong, S., Katz, B., Kushnir, D., & Prieto, J. L. 2015, MNRAS, 454, L61, doi: 10.1093/mnrasl/slv129

Drake, A. J., Djorgovski, S. G., Mahabal, A., et al. 2009, ApJ, 696, 870, doi: 10.1088/0004-637X/696/1/870

Fakhouri, H. K., Boone, K., Aldering, G., et al. 2015, ApJ, 815, 58, doi: 10.1088/0004-637X/815/1/58

Feindt, U., Kerschhaggl, M., Kowalski, M., et al. 2013, A&A, 560, A90, doi: 10.1051/0004-6361/201321880

Filippenko, A. V., Richmond, M. W., Matheson, T., et al. 1992a, ApJL, 384, L15, doi: 10.1086/186252

Filippenko, A. V., Richmond, M. W., Branch, D., et al. 1992b, AJ, 104, 1543, doi: 10.1086/116339

Folatelli, G., Morrell, N., Phillips, M. M., et al. 2013, ApJ, 773, 53, doi: 10.1088/0004-637X/773/1/53

Foley, R. J., Hoffmann, S. L., Macri, L. M., et al. 2020, MNRAS, 491, 5991, doi: 10.1093/mnras/stz3324

Foley, R. J., Narayan, G., Challis, P. J., et al. 2010a, ApJ, 708, 1748, doi: 10.1088/0004-637X/708/2/1748

—. 2010b, ApJ, 708, 1748, doi: 10.1088/0004-637X/708/2/1748

Foley, R. J., Challis, P. J., Chornock, R., et al. 2013, ApJ, 767, 57, doi: 10.1088/0004-637X/767/1/57

Galbany, L., Anderson, J. P., Rosales-Ortega, F. F., et al. 2016, MNRAS, 455, 4087, doi: 10.1093/mnras/stv2620

Galbany, L., Ashall, C., Höflich, P., et al. 2019, A&A, 630, A76, doi: 10.1051/0004-6361/201935537

Gall, C., Stritzinger, M. D., Ashall, C., et al. 2018, A&A, 611, A58, doi: 10.1051/0004-6361/201730886

Gall, E. E. E., Taubenberger, S., Kromer, M., et al. 2012, MNRAS, 427, 994, doi: 10.1111/j.1365-2966.2012.21999.x

Garavini, G., Folatelli, G., Nobili, S., et al. 2007, A&A, 470, 411, doi: 10.1051/0004-6361:20065400

Hamuy, M., Phillips, M. M., Suntzeff, N. B., et al. 1996, AJ, 112, 2391, doi: 10.1086/118190

—. 2003, Nature, 424, 651, doi: 10.1038/nature01854

Hamuy, M., Folatelli, G., Morrell, N. I., et al. 2006, PASP, 118, 2, doi: 10.1086/500228

Hicken, M., Garnavich, P. M., Prieto, J. L., et al. 2007, ApJL, 669, L17, doi: 10.1086/523301

Hoeflich, P., & Khokhlov, A. 1996, ApJ, 457, 500, doi: 10.1086/176748

Höflich, P., Gerardy, C. L., Fesen, R. A., & Sakai, S. 2002, ApJ, 568, 791, doi: 10.1086/339063

Howell, D. A., Sullivan, M., Nugent, P. E., et al. 2006, Nature, 443, 308, doi: 10.1038/nature05103

Howerton, S. 2016, Transient Name Server Discovery Report, 2016-157, 1

Hoyle, F., & Fowler, W. A. 1960, ApJ, 132, 565, doi: 10.1086/146963

Hsiao, E. Y., Marion, G. H., Phillips, M. M., et al. 2013, ApJ, 766, 72, doi: 10.1088/0004-637X/766/2/72

Hsiao, E. Y., Burns, C. R., Contreras, C., et al. 2015, A&A, 578, A9, doi: 10.1051/0004-6361/201425297

Hsiao, E. Y., Phillips, M. M., Marion, G. H., et al. 2019, PASP, 131, 014002, doi: 10.1088/1538-3873/aae961

Hsiao, E. Y., Hoeflich, P., Ashall, C., et al. 2020, ApJ, 900, 140, doi: 10.3847/1538-4357/abaf4c

Iben, I., J., & Tutukov, A. V. 1984, ApJS, 54, 335, doi: 10.1086/190932

Jack, D., Baron, E., & Hauschildt, P. H. 2015, MNRAS, 449, 3581, doi: 10.1093/mnras/stv474

Jensen, J. B., Blakeslee, J. P., Ma, C.-P., et al. 2021, arXiv e-prints, arXiv:2105.08299. https://arxiv.org/abs/2105.08299

Jha, S., Kirshner, R. P., Challis, P., et al. 2006, AJ, 131, 527, doi: 10.1086/497989

Kasen, D. 2006, ApJ, 649, 939, doi: 10.1086/506588

Katz, B., & Dong, S. 2012, arXiv e-prints, arXiv:1211.4584. https://arxiv.org/abs/1211.4584

Kelly, P. L., Hicken, M., Burke, D. L., Mandel, K. S., & Kirshner, R. P. 2010, ApJ, 715, 743, doi: 10.1088/0004-637X/715/2/743

Khetan, N., Izzo, L., Branchesi, M., et al. 2021, A&A, 647, A72, doi: 10.1051/0004-6361/202039196

Kochanek, C. S., Shappee, B. J., Stanek, K. Z., et al. 2017, PASP, 129, 104502, doi: 10.1088/1538-3873/aa80d9
Kowalski, M., Rubin, D., Aldering, G., et al. 2008, ApJ, 686, 749, doi: 10.1086/589937
Krisciunas, K., Contreras, C., Burns, C. R., et al. 2017, AJ, 154, 211, doi: 10.3847/1538-3881/aa8df0
Kushnir, D., Katz, B., Dong, S., Livne, E., & Fernández, R. 2013, ApJL, 778, L37, doi: 10.1088/2041-8205/778/2/L37
Lampeitl, H., Smith, M., Nichol, R. C., et al. 2010, ApJ, 722, 566, doi: 10.1088/0004-637X/722/1/566
Leibundgut, B., Kirshner, R. P., Phillips, M. M., et al. 1993, AJ, 105, 301, doi: 10.1086/116427
Leloudas, G., Stritzinger, M. D., Sollerman, J., et al. 2009, A&A, 505, 265, doi: 10.1051/0004-6361/200912364
Li, W., Filippenko, A. V., Chornock, R., et al. 2003, PASP, 115, 453, doi: 10.1086/374200
Li, W., Leaman, J., Chornock, R., et al. 2011, MNRAS, 412, 1441, doi: 10.1111/j.1365-2966.2011.18160.x
Li, W. D., Qiu, Y. L., Qiao, Q. Y., et al. 1997, IAUC, 6661, 1
Livne, E. 1990, ApJL, 354, L53, doi: 10.1086/185721
López-Cobá, C., Sánchez, S. F., Anderson, J. P., et al. 2020, AJ, 159, 167, doi: 10.3847/1538-3881/ab7848
Lu, J., Ashall, C., Hsiao, E. Y., et al. 2021, arXiv e-prints, arXiv:2107.08150. https://arxiv.org/abs/2107.08150
Marion, G. H., Höflich, P., Gerardy, C. L., et al. 2009, AJ, 138, 727, doi: 10.1088/0004-6256/138/3/727
Mazzali, P. A., Ashall, C., Pian, E., et al. 2018, MNRAS, 476, 2905, doi: 10.1093/mnras/sty434
Mazzali, P. A., Chugai, N., Turatto, M., et al. 1997, MNRAS, 284, 151, doi: 10.1093/mnras/284.1.151
Mazzali, P. A., Röpke, F. K., Benetti, S., & Hillebrandt, W. 2007, Science, 315, 825, doi: 10.1126/science.1136259
Nomoto, K. 1980, in Texas Workshop on Type I Supernovae, ed. J. C. Wheeler, 164–181
Nomoto, K., Iwamoto, K., Nakasato, N., et al. 1997, NuPhA, 621, 467, doi: 10.1016/S0375-9474(97)00291-1
Nugent, P., Phillips, M., Baron, E., Branch, D., & Hauschildt, P. 1995, ApJL, 455, L147, doi: 10.1086/309846
Nugent, P. E., Sullivan, M., Cenko, S. B., et al. 2011, Nature, 480, 344, doi: 10.1038/nature10644
Pastorello, A., Mazzali, P. A., Pignata, G., et al. 2007, MNRAS, 377, 1531, doi: 10.1111/j.1365-2966.2007.11700.x
Pejcha, O., Antognini, J. M., Shappee, B. J., & Thompson, T. A. 2013, MNRAS, 435, 943, doi: 10.1093/mnras/stt1281
Perlmutter, S., Aldering, G., Goldhaber, G., et al. 1999, ApJ, 517, 565, doi: 10.1086/307221
Phillips, M. M. 1993, ApJL, 413, L105, doi: 10.1086/186970
—. 2012, PASA, 29, 434, doi: 10.1071/AS11056
Phillips, M. M., Lira, P., Suntzeff, N. B., et al. 1999, AJ, 118, 1766, doi: 10.1086/301032
Phillips, M. M., Wells, L. A., Suntzeff, N. B., et al. 1992, AJ, 103, 1632, doi: 10.1086/116177
Phillips, M. M., Phillips, A. C., Heathcote, S. R., et al. 1987, PASP, 99, 592, doi: 10.1086/132020
Phillips, M. M., Contreras, C., Hsiao, E. Y., et al. 2019, PASP, 131, 014001, doi: 10.1088/1538-3873/aae8bd
Piersanti, L., Gagliardi, S., Iben, Icko, J., & Tornambé, A. 2003, ApJ, 598, 1229, doi: 10.1086/378952
Poznanski, D., Prochaska, J. X., & Bloom, J. S. 2012, MNRAS, 426, 1465, doi: 10.1111/j.1365-2966.2012.21796.x
Raiteri, C. M., Villata, M., & Navarro, J. F. 1996, A&A, 315, 105
Raskin, C., Timmes, F. X., Scannapieco, E., Diehl, S., & Fryer, C. 2009, MNRAS, 399, L156, doi: 10.1111/j.1745-3933.2009.00743.x
Riess, A. G., Filippenko, A. V., Challis, P., et al. 1998, AJ, 116, 1009, doi: 10.1086/300499
Riess, A. G., Macri, L. M., Hoffmann, S. L., et al. 2016, ApJ, 826, 56, doi: 10.3847/0004-637X/826/1/56
Rosswog, S., Kasen, D., Guillochon, J., & Ramirez-Ruiz, E. 2009, ApJL, 705, L128, doi: 10.1088/0004-637X/705/2/L128
Schlafly, E. F., & Finkbeiner, D. P. 2011, ApJ, 737, 103, doi: 10.1088/0004-637X/737/2/103
Scolnic, D. M., Jones, D. O., Rest, A., et al. 2018, ApJ, 859, 101, doi: 10.3847/1538-4357/aab9bb
Shappee, B. J., & Thompson, T. A. 2013, ApJ, 766, 64, doi: 10.1088/0004-637X/766/1/64
Shappee, B. J., Prieto, J. L., Grupe, D., et al. 2014, ApJ, 788, 48, doi: 10.1088/0004-637X/788/1/48
Simien, F., & Prugniel, P. 1997, A&AS, 126, 15, doi: 10.1051/aas:1997247
Smartt, S. J., Valenti, S., Fraser, M., et al. 2015, A&A, 579, A40, doi: 10.1051/0004-6361/201425237
Stritzinger, M., Leibundgut, B., Walch, S., & Contardo, G. 2006, A&A, 450, 241, doi: 10.1051/0004-6361:20053652
Stritzinger, M., Burns, C. R., Phillips, M. M., et al. 2010, AJ, 140, 2036, doi: 10.1088/0004-6256/140/6/2036
Sullivan, M., Conley, A., Howell, D. A., et al. 2010, MNRAS, 406, 782, doi: 10.1111/j.1365-2966.2010.16731.x
Szabó, G. M., Sárneczky, K., Vinkó, J., et al. 2003, A&A, 408, 915, doi: 10.1051/0004-6361:20031008
Taubenberger, S. 2017, The Extremes of Thermonuclear Supernovae, ed. A. W. Alsabti & P. Murdin, 317, doi: 10.1007/978-3-319-21846-5_37

Thompson, T. A. 2011, ApJ, 741, 82, doi: 10.1088/0004-637X/741/2/82

Turatto, M., Benetti, S., Cappellaro, E., et al. 1996, MNRAS, 283, 1, doi: 10.1093/mnras/283.1.1

Turatto, M., Piemonte, A., Benetti, S., et al. 1998a, AJ, 116, 2431, doi: 10.1086/300622

—. 1998b, AJ, 116, 2431, doi: 10.1086/300622

van den Bosch, R. C. E., Gebhardt, K., Gültekin, K., Yıldırım, A., & Walsh, J. L. 2015, ApJS, 218, 10, doi: 10.1088/0067-0049/218/1/10

van Kerkwijk, M. H., Chang, P., & Justham, S. 2010, ApJL, 722, L157, doi: 10.1088/2041-8205/722/2/L157

Webbink, R. F. 1984, ApJ, 277, 355, doi: 10.1086/161701

Wheeler, J. C., Höflich, P., Harkness, R. P., & Spyromilio, J. 1998, ApJ, 496, 908, doi: 10.1086/305427

Whelan, J., & Iben, Icko, J. 1973, ApJ, 186, 1007, doi: 10.1086/152565

Woosley, S. E., & Weaver, T. A. 1994, ApJ, 423, 371, doi: 10.1086/173813

Yamanaka, M., Kawabata, K. S., Kinugasa, K., et al. 2009, ApJL, 707, L118, doi: 10.1088/0004-637X/707/2/L118

Yaron, O. 2017, Transient Name Server Classification Report, 2017-705, 1